

1 **Fault Growth and Interactions in a Multiphase Rift Fault Network: Horda**
2 **Platform, Norwegian North Sea**

3
4 **Oliver B. Duffy^{1*}, Rebecca E. Bell¹, Christopher A-L. Jackson¹, Rob L. Gawthorpe², Paul S.**
5 **Whipp³**
6

7 ¹*Basins Research Group (BRG), Department of Earth Science & Engineering, Imperial College, Prince*
8 *Consort Road, London, United Kingdom, SW7 2BP*

9 ²*Department of Earth Science, University of Bergen, P.O. Box 7803, N-5020 Bergen, Norway*

10 ³*Statoil ASA, Sandslivegen 90, 5254 Sandslid, Norway*

11 **Present Address of Corresponding Author: Bureau of Economic Geology, Jackson School of*
12 *Geosciences, The University of Texas at Austin, University Station, Box X, Austin, Texas, 78713-8924,*
13 *USA (e-mail: oliver.duffy@beg.utexas.edu)*

14
15 Running Title: Fault Growth Characteristics in Multiphase Rifts

16 Keywords: normal faulting, multiphase rifting, fault growth, fault interactions, fault throw, fault
17 networks, North Sea

18 **Word Count: ca. 8500** (without abstract and acknowledgements)

19 **Abstract:**

20 Physical models predict that multiphase rifts that experience a change in extension direction between
21 stretching phases will typically develop non-colinear normal fault sets. Furthermore, multiphase rifts
22 will display a greater frequency and range of styles of fault interactions than single-phase rifts.
23 Although these physical models have yielded useful information on the evolution of fault networks in
24 map view, the true 3D geometry of the faults and associated interactions are poorly understood. Here,
25 we use an integrated 3D seismic reflection and borehole dataset to examine a range of fault
26 interactions that occur in a natural multiphase fault network in the northern Horda Platform, northern
27 North Sea. In particular we aim to: i) determine the range of styles of fault interaction that occur
28 between non-colinear faults; ii) examine the typical geometries and throw patterns associated with
29 each of these different styles; and iii) highlight the differences between single-phase and multiphase
30 rift fault networks. Our study focuses on a ca. 350 km² region around the >60 km long, N-S-striking

31 Tusse Fault, a normal fault system that was active in the Permian-Triassic and again in the Late
32 Jurassic-to-Early Cretaceous. The Tusse Fault is one of a series of large (>1500 m throw) N-S-striking
33 faults forming part of the northern Horda Platform fault network, which includes numerous smaller
34 (2-10 km long), lower throw (<100 m), predominantly NW-SE-striking faults that were only active
35 during the Late Jurassic to Early Cretaceous. We examine how the 2nd-stage NW-SE-striking faults
36 grew, interacted and linked with the N-S-striking Tusse Fault, documenting a range of interaction
37 styles including mechanical and kinematic isolation, abutment, retardation and reactivated relays. Our
38 results demonstrate that: i) isolated, non-interacting and abutting interactions are the most common
39 fault interaction styles in the northern Horda Platform; ii) pre-existing faults can act as sites of
40 nucleation for 2nd-stage faults or may form mechanical barriers to propagation; iii) the throw
41 distribution on reactivated 1st-stage faults will be modified in a predictable manner if they are
42 intersected or influenced by 2nd-stage faults; iv) sites of fault linkage and relay-breaching associated
43 with the first phase of extension can act as preferential nucleation sites for 2nd-stage faults; and v) the
44 development of fault intersections is a dynamic process, involving the gradual transition from one
45 style to another.

46

47 **1. Introduction**

48

49 Faults that develop during a single phase of extension typically strike sub-perpendicular to the
50 extension direction and show an en échelon or colinear configuration (e.g. Gawthorpe and Leeder,
51 2000) (*Fig 1*). Faults with strikes that are oblique to the main rift trend (herein termed ‘non-colinear
52 faults’) can also develop during a single rift phase, commonly due to breaching of relay zones (e.g.
53 Trudgill et al., 2002), flexure and gravity-driven sliding of the cover above weak layers (e.g.
54 overpressured mudstone or and salt; e.g. Stewart and Clark, 1999) and the development of ‘release’
55 faults (e.g. Destro, 1995). Furthermore, non-colinear faults also develop in response to: i)
56 perturbations in the local stress field around pre-existing or broadly synchronous normal faults

57 (Maerten et al., 1999; 2002); ii) compaction and dewatering, which in some cases leads to radially-
58 isotropic strain expressed as ‘polygonal’ faulting (e.g. Cartwright and Lonergan, 1996; Cartwright and
59 Dewhurst, 1998); and iii) the anisotropic effects of pre-existing fabrics that are oriented obliquely to
60 the extension direction (e.g. Morley et al., 2004) (*Fig. 1*; see also Reeve et al., 2015 for a synthesis).
61 However, the development of non-colinear faults in many of these cases is not pervasive across the
62 fault network and the range of styles of interaction and overall influence of fault interactions in the
63 evolution of the fault network is relatively low (*Fig. 1*).

64 In contrast, in multiphase rifts, and particularly where the extension direction during each rift
65 phase differs, faults formed in the first rift phase influence how strain is accommodated in the upper
66 crust in the second rift phase (e.g. Keep and McClay, 1997; Bellahsen and Daniel, 2005; Henza et al.,
67 2011; Whipp et al., 2014). In this situation the later rift phase is characterised by reactivation of pre-
68 existing faults from the 1st-rift stage and/or nucleation of newly formed, 2nd-stage faults in previously
69 unruptured crust, which generally strike sub-perpendicular to the new extension direction (e.g. Bailey
70 et al., 2005; Henza et al., 2010; 2011; Whipp et al., 2014). Fault networks in multiphase rifts are
71 therefore prone to comprise of pervasive non-colinear fault sets, with interaction and intersections
72 between the non-colinear faults common, as is observed in the Jeanne D’Arc rift (e.g. Sinclair and
73 Withjack, 2008), Gulf of Aden (Bellahsen et al., 2006), Gulf of Thailand (e.g. Morley et al., 2004,
74 2007), Alaska (Nixon et al., 2014) and the North Sea (Badley et al., 1998; Færseth, 1996; Odinsen et
75 al., 2000; Whipp et al., 2014).

76 Much of our understanding of how non-colinear faults and fault interactions evolve in multiphase
77 rifts is based on predictions from physical models (e.g. McClay and White, 1995; Bellahsen and
78 Daniel, 2005; Henza et al., 2010; 2011; Chattopadhyay and Chakra, 2013). While these physical
79 models provide important information on the plan-view evolution of faults and fault interactions, the
80 true 3D geometry of the faults and interaction styles remain unknown. Furthermore, there is a general
81 lack of observations of different fault interaction styles from outcrop or subsurface natural examples,
82 although Nelson (2006) and Nixon et al. (2014) provide notable exceptions.

83 In this study we examine a fault network in a natural multiphase rift to: i) identify a range of
84 styles of fault interaction and/or linkage between 1st and 2nd-stage faults; ii) examine the tipline

85 geometries, branchline characteristics and throw patterns associated with each interaction style; and
86 iii) develop an understanding of how fault interaction styles evolve. To achieve this we integrate
87 observations from a 3D seismic reflection and borehole dataset that covers the northern Horda
88 Platform array, Horda Platform, northern North Sea. This setting is ideal for this study because
89 previous studies demonstrate the area was subject to two rift events, which resulted in the formation
90 of fault sets with different dominant strikes (Badley et al., 1998; Færseth, 1996; Odinsen et al., 2000;
91 Whipp et al., 2014). Furthermore, the relatively shallow burial of the area means faults and
92 branchlines are well-imaged, and an abundance of borehole data allows us to constrain the age of
93 growth strata adjacent to the faults, and hence constrain the temporal evolution of the fault array.
94 Using this information, we improve our understanding of how pre-existing faults influence the
95 development of subsequent fault networks and present a template of fault interaction styles that will
96 aid structural mapping in seismic datasets lacking such clear imaging of faults and their geometric
97 relationships.

98

99 **2. Geological Framework**

100

101 ***2.1 Regional Tectonic Evolution***

102 The crystalline basement of the northern North Sea was influenced by contractional episodes in the
103 Caledonian (460-400 Ma) and Variscan (400-300 Ma) orogenies (e.g. Ziegler, 1975). During the
104 Devonian, post-orogenic crustal relaxation resulted in the development of major extensional shear
105 zones and intermontane basins, such as those preserved onshore western Norway (e.g. Fossen, 1992;
106 Vetti and Fossen, 2012). These extensional shear zones formed a crustal fabric which is interpreted to
107 have influenced the development of the North Sea basin by modifying the geometry of Mesozoic rift
108 systems and influencing the distribution of thermally-driven Cenozoic subsidence (e.g. Glennie et al,
109 1987; Ziegler, 1990; Stewart et al., 1992; Bartholomew et al., 1993; Smethurst, 2000).

110 The first main rift phase (herein termed ‘Rift Phase 1’) initiated in the Late Permian and
111 continued for 25-37 Myr before ceasing in the Early Triassic (e.g. Ziegler, 1982; Ziegler, 1990; 1992;

112 Ter Voorde et al., 2000). Based on the prevalence of large displacement (3-5 km), N-S-striking
113 Permian-Triassic fault systems, an E-W extension direction is inferred for Rift Phase 1 (Færseth,
114 1996; Færseth et al., 1997) (*Fig. 2*). Faults developed during Rift Phase 1 dip predominantly westward
115 and bound easterly-tilted half-grabens (e.g. Færseth, 1996; Bell et al., 2014) (*Fig. 2*).

116 Following a *ca.* 70 Ma period of relative tectonic quiescence and post-rift thermal subsidence,
117 a second rift phase (herein termed ‘Rift Phase 2’) initiated in the Middle Jurassic (e.g. Badley et al.,
118 1988; Underhill and Partington, 1993; Roberts et al., 1995; Coward et al., 2003; Cowie et al., 2005)
119 (*Fig. 3*). Rift Phase 2 continued until the Early Cretaceous, although the onset and cessation of active
120 faulting across the rift was diachronous (e.g. Coward et al., 2003; Cowie et al., 2005; Bell et al.,
121 2014). Currently, no consensus exists on the direction of extension during Rift Phase 2 in the northern
122 North Sea; some studies invoke a continuation of the E-W extension experienced in Rift Phase 1 (e.g.
123 Stewart et al., 1992; Bartholomew et al., 1993; Brun and Tron, 1993) whereas others propose a
124 rotation of the extension direction to either NW-SE, WNW-ESE or NNE-SSW (e.g. Ziegler, 1990,
125 1992; Færseth, 1996; Dore et al., 1997; Færseth et al., 1997; Davies et al., 2001). Once Rift Phase 2
126 ceased, the northern North Sea experienced post-rift thermal subsidence, which was focused in the
127 axis of the Viking Graben (Odinsen et al., 2000).

128 The magnitudes of extension experienced in Rift Phases 1 and 2 were broadly similar
129 (stretching factors of 1.4-1.5; Roberts et al., 1993; Færseth, 1996; Odinsen et al., 2000), although the
130 way in which extension was distributed varied between phases. Some authors think that, during Rift
131 Phase 1, extension was distributed evenly across the rift (Odinsen et al., 2000) whereas other postulate
132 that extension was greatest in the region that is the present-day Horda Platform (Færseth, 1996; Ter
133 Voorde et al., 2000). In contrast, during Rift Phase 2, extension in the northern North Sea was focused
134 in the Viking Graben (Odinsen et al., 2000; Cowie et al., 2005).

135

136 ***2.2. Geological Setting of the Horda Platform***

137 The Horda Platform is a *ca.* 300 km long, N-S-trending structural high located along the eastern
138 margin of the Norwegian North Sea, bounded to the west by the North Viking Graben and to the east

139 by the Øygarden Fault Complex (e.g. Færseth, 1996; Bell et al., 2014; Whipp et al., 2014) (*Fig. 2*).
140 The northern part of the platform is dissected by a fault network that comprises a N-S-striking fault
141 set active during both Rift Phases 1 and 2, and a broadly NW-SE-striking set that was only active
142 during Rift Phase 2 (*Fig. 2*) (Whipp et al., 2014). The N-S-striking, basement-involved faults, which
143 include the Svartav, Tusse, Vette and Øygarden fault systems, dip westward, are up to >60 km long
144 and have an average spacing of *ca.* 6-15 km (*Fig. 2*) (Whipp et al., 2014). These faults have up to 5
145 km of throw and define east-tilted half grabens filled with up to 3 km of Permo-Triassic sediments
146 (e.g. Færseth, 1996; Bell et al., 2014; Whipp et al., 2014) (*Fig. 2*). In contrast, the NW-SE-striking
147 faults are short (2-10 km), have low displacement (30-100 m), are closely-spaced (0.5-5 km), and are
148 stratabound, being restricted to post-Upper Triassic stratigraphy (*Fig. 2*) (Whipp et al., 2014).

149 During the Triassic, the Horda Platform experienced continental conditions, resulting in the
150 deposition of sandstones and mudstones (e.g. Hegre Group; *Fig. 3*) (Lervik, 2006). In the Early
151 Jurassic to early Middle Jurassic, fluvio-deltaic-to-shallow-marine sediments of the Staffjord
152 Formation, and Dunlin and Brent groups were deposited, during a period of tectonic quiescence and
153 post-rift thermal subsidence following Rift Phase 1; *Fig. 3*) (e.g. Helland-Hansen et al., 1992). The
154 diachronous onset of Rift Phase 2 was, in some places, coincident with deposition of the uppermost
155 part of the Brent Group (*Fig. 3*) (e.g. Helland-Hansen et al., 1992). An overall deepening of the basin,
156 which was associated with increased fault-controlled subsidence in Rift Phase 2, led to the deposition
157 of the fully-marine Viking Group (*Fig. 3*). On the Horda Platform this consists of three stacked
158 shallow marine clastic wedges, the Krossfjord, Fensfjord and Sognefjord formations, which are
159 separated by major marine flooding events (*Fig. 3*) (e.g. Dreyer et al., 2005; Holgate et al., 2013).
160 Basinwide flooding during the Late Kimmeridgian to Late Berriasian led to the deposition of marine
161 mudstones of the Draupne Formation, which is capped by the Base Cretaceous Unconformity (BCU)
162 (*Fig. 3*) (e.g. Rattey et al., 1993; Kyrkjebo et al., 2004). The clastic-dominated Jurassic stratigraphy
163 was shallowly buried and thus likely weakly lithified at the onset of Rift Phase 2 extension, thus
164 extensional forced folds and 'drag'-related folds are common in these units (Whipp et al., 2014). The
165 BCU is overlain by deep-water clastics and carbonates (Cromer Knoll and Shetland groups), which

166 are, in turn, overlain by a mud-dominated Cenozoic succession (*Fig. 3*) (e.g. Lepercq and Gaulier,
167 1996).

168

169 **3. Dataset and Methodology**

170

171 This study focuses on a *ca.* 350 km² region around the Tusse Fault System, in an area covered by 2D
172 and 3D time-migrated seismic reflection surveys (*Fig. 2*). The seismic data are zero-phase and reverse
173 polarity (SEG convention) with seismic sections presented such that troughs (blue reflections)
174 represent a downward increase in acoustic impedance. The 3D survey on which the majority of the
175 fault and horizon interpretation is based has a vertical sampling interval of 2 milliseconds two-way
176 time (ms TWT) and a record length of 3000 ms TWT, with inlines (NE-trending) and crosslines (NW-
177 trending) spaced 18.75 m and 12.48 m, respectively. Within the Top Triassic to Early Cretaceous
178 interval of interest, the 3D seismic survey has a dominant frequency of *ca.* 50 Hz, thus, by assuming
179 an average seismic velocity of 2000 m/s TWT we determine a vertical seismic resolution or ‘limit of
180 separability’ (1/4 wavelength) of *ca.* 10 m. The shallow burial of the Horda Platform means that the
181 resolution of the 3D data is sufficient for detailed fault and horizon mapping. The 2D seismic lines are
182 spaced approximately 1 km, have a record length of 5000-7000 ms TWT, and are used mainly to
183 constrain the thickness of the Permian-Triassic succession and the depth to acoustic basement (*Fig.*
184 *2a*).

185 Eight key seismic surfaces, spanning the pre-, syn- and post-rift intervals, were identified
186 based on stratal terminations and marked changes in seismic facies; these surfaces were mapped
187 across the study area (*Fig. 3*) and were tied to eighteen wells using synthetic seismograms that helped
188 constrain their ages (see Whipp et al., 2014). Faults, tiplines and branchlines were mapped on closely-
189 spaced seismic sections, with care taken to accurately constrain fault-horizon cut-offs. Note that the
190 term ‘branchline’ is used to define any line that joins two fault planes, irrespective of kinematic or age
191 relationships between the faults. Styles of interaction and linkage between the non-colinear fault sets

192 were identified and the geometry and kinematics of each style were examined in turn using evidence
193 from TWT structure maps, isochron maps and seismic sections.

194 To determine how each interaction or linkage style evolved, we followed the approach of
195 Nelson (2006) by defining the geometry of the faults, tiplines and branchlines before systematically
196 examining throw patterns. First, to constrain how throw is distributed along-strike of key faults,
197 throw-distance ($T-x$) measurements were taken on different structural surfaces (e.g. Peacock and
198 Sanderson, 1991). Second, to establish fault growth histories, throw-depth ($T-z$) plots were
199 constructed, where throw across faulted horizons is plotted against the depth to the midpoint between
200 the respective hanging-wall and footwall cut-offs (e.g. Muraoka and Kamata, 1983; Cartwright et al.,
201 1995; Hongxing and Anderson, 2007; Baudon and Cartwright 2008a, b and c; Pochat et al., 2009).
202 Third, throw strike projections (cf. Walsh and Watterson, 1991) were constructed for key faults to
203 highlight the 3D distribution of throw at sites of interaction and linkage (see methods of Nelson, 2006;
204 Baudon and Cartwright, 2008a, b and c). Throw values were converted from time (ms TWT) to depth
205 (m) using a velocity model derived from time-depth curves from seven wells located within 6 km of
206 the Tusse Fault. These wells show a simple best-fit second-order polynomial relationship between
207 time and depth with an error margin of 50-120 m at the depth of interest (*Fig. 2 and Appendix 1*; see
208 methods of Whipp et al., 2014; Bell et al., 2014). Patterns of throw on the faults do not vary
209 significantly between the time and depth domains due to simple velocity structure in the overburden
210 (cf. Baudon and Cartwright, 2008c; Conneally et al., 2014).

211 Unless otherwise stated in the text, the effect of fault-parallel folding on fault throw has been
212 removed, such that total strain across the fault is calculated, whether accommodated by ductile
213 (continuous) or brittle (discontinuous) deformation (e.g. Meyer et al., 2002; Long and Imber, 2010;
214 Whipp et al., 2014). To achieve this, cut-offs were defined using an extrapolated line that follows the
215 regional trend of the horizon prior to folding (e.g. Chapman and Meneilly, 1991; Mansfield and
216 Cartwright, 1996; Wilson et al., 2013).

217

218 **4. Overview of the Northern Horda Platform Fault Network**

219

220 The Top Sognefjord TWT-structure map best illustrates the geometry of the Northern Horda Platform
221 fault network because it records deformation associated with both reactivated Permian-Triassic faults
222 and new Middle Jurassic-Early Cretaceous faults (*Fig. 4a*). The Top Sognefjord horizon lies just
223 below the Rift Phase 2 pre-rift /syn-rift contact. Deformation is dominated by the N-S-striking, W-
224 dipping Tusse Fault, along with a series of shorter, predominantly NW-SE-striking faults that are
225 present in both the hanging-wall and footwall of the Tusse Fault (*Fig. 4a*). These smaller faults show
226 varying degrees and styles of mechanical interaction and/or linkage with the Tusse Fault, including
227 examples that are: i) isolated and non-interacting; ii) abutting; iii) exploiting relay-breaching faults;
228 and iv) retarded (*Fig. 4a*).

229 In plan view, the Tusse Fault is >33 km long, curvilinear and has an overall N-S strike,
230 although some small portions of the fault strike NE-SW or NW-SE (*Fig. 4a*). On dip-oriented cross-
231 sections, the fault is basement-rooted with the upper tip typically located in uppermost Cretaceous or
232 Tertiary strata, being overlain by a west-facing monocline (*Fig. 5a*). Throw is highest at the Top
233 Basement structural surface (>1400 ms), whereas at the Top Sognefjord structural surface, throw is
234 smaller 120-700 m (90-520 ms TWT) (*Fig. 5a*). Throw does not vary smoothly along-strike of the
235 Tusse Fault; instead, throw variations are 'step-like', and, locally, of large magnitude (up to 500 m)
236 (*Fig. 4b*). These 'steps' in throw correlate with locations where: i) NW-SE-striking 2nd-stage faults
237 mechanically interact or link with the Tusse Fault; and ii) there are significant changes in the
238 magnitude of ductile deformation, calculated by subtracting the true throw from the projected throw,
239 along-strike of the Tusse Fault (*Fig. 4; see sections 5 and 6*).

240 Permian-Triassic and mid-Upper Jurassic to Lower Cretaceous strata thicken towards the
241 Tusse Fault (*Figs. 5a and 6*) and *T-z* profiles, taken at a range of locations along the Tusse Fault
242 (including near sites of linkage with NW-SE-striking faults), show that, for both of these intervals of
243 growth strata, throw increases with depth (*Fig. 7a*). These observations suggest the Tusse Fault was
244 an active surface-breaking fault during Rift Phases 1 and 2 (see also Whipp et al., 2014). In contrast,
245 the intervening Lower to mid-Upper Jurassic interval displays a relatively tabular geometry (*Figs. 5a*

246 *and 6*) and shows little variation in throw with depth (*Fig. 7a*). As such, we interpret that faulting in
247 this interval is post-sedimentary and the Early to mid-Late Jurassic was a time of fault inactivity and
248 burial (see also Whipp et al., 2014).

249 At the Top Sognefjord level, the broadly NW-SE-striking faults are typically 1-8 km long and
250 are mainly linear in map view, although some faults in the south of the study area curve to strike N-S
251 in the immediate hanging-wall of the Tusse Fault (*Fig. 4a*). Fault throw is typically 30-100 m (*ca.* 20–
252 70 ms TWT) (*Fig. 5b*), but locally up to 300 m (*ca.* 210 ms TWT). On time-migrated cross-sections,
253 the faults are planar with lower tips commonly located in uppermost Triassic sediments and upper tips
254 located in the Cretaceous or lowermost Tertiary succession (*Fig. 5*). Thus it is unlikely that: i)
255 structures or fabrics in the pre-Permian basement had any direct influence on the growth of the NW-
256 SE-striking faults; or ii) lower faults were simply reactivated to form the upper faults.

257 Lower Cretaceous strata thicken towards most but not all of the NW-SE-striking faults,
258 suggesting some faults were active and broke surface during this time (*Figs. 5 and 6*). *T-z* profiles
259 constructed for some of the NW-SE-striking faults are broadly symmetrical or slightly skewed
260 towards the upper tip (*cf.* ‘C-type’ profiles of Muraoka and Kamata; 1983) (*Fig. 7b*). The points of
261 maximum throw on *T-z* profiles, often interpreted to represent the sites of fault nucleation of the fault
262 (Mansfield and Cartwright, 1996; Cartwright et al., 1998; Hongxing and Anderson, 2007), are
263 typically located at the Top Sognefjord (mid-Upper Jurassic) stratigraphic level, with throw
264 decreasing to the upper and lower tips (*Fig. 7b*). We therefore interpret that the NW-SE-striking faults
265 nucleated in the mid Upper Jurassic succession, were only active during Rift Phase 2, and developed
266 mainly as a population of surface-breaking faults with some faults remaining blind (see also Whipp et
267 al., 2014).

268

269 **5. Fault Interaction and Linkage Styles**

270 Here we examine variations in the fault tipline geometry, kinematics and throw patterns associated
271 with each of the styles of interaction and linkage that occur between the Tusse Fault and 2nd-stage
272 NW-SE-striking faults (F1-F16 on Fig 4). We initially examine mechanically and kinematically

273 isolated 2nd-stage faults (section 5.1), and then examples where 2nd-stage faults abut against the Tusse
274 Fault at relatively simple branchlines (section 5.2). We conclude by describing more complex styles,
275 for example where 2nd-stage faults appear to reactivate 1st-stage relay-breaching faults (section 5.3)
276 or show evidence of being mechanically retarded by the Tusse Fault (sections 5.3 and 5.4,
277 respectively). For each of these styles, the plan-view structural style is described at the Upper Jurassic
278 Top Sognefjord TWT structural surface. Furthermore, it is assumed that general characteristics (e.g.
279 periods faults were active and/or surface-breaking, upper and lower tip locations, stratigraphic level of
280 nucleation) of the Tusse Fault and the 2nd-stage NW-SE-striking faults (F1-F16) respectively, are the
281 same as the type examples described in section 4. This section focuses on how interactions between
282 the non-colinear faults influence throw patterns as well as tipline and branchline geometry.

283

284 ***5.1. Mechanically and Kinematically Isolated Faults***

285 Fault F11 is representative of the numerous 2nd-stage NW-SE-striking normal faults that are isolated,
286 that is, they show no evidence of interaction or linkage with other NW-SE-striking faults or the Tusse
287 Fault. Fault F11 has a linear trace in map view, dips to the NE and lies *ca.* 7 km into the hangingwall
288 of the Tusse Fault (*Figs. 4a, 5c, 8a*). The tipline of F11 is quasi-elliptical with a flat upper tipline
289 located in the lowermost Tertiary succession (*Fig. 8c*) and a lower tipline located in the uppermost
290 Triassic interval. Maximum fault height at the centre of the fault ellipse is *ca.* 980 m (*ca.* 900 ms
291 TWT) (*Fig. 8c*).

292 *T-x* profiles are smooth and symmetrical, with throw highest at the centre of the fault (*Fig.*
293 *8b*). On the fault surface, throw contours are quasi-elliptical and show a ‘bullseye’ pattern, centred on
294 a single throw maximum (*ca.* 65-70 m or 50 ms TWT) that is located towards the upper centre of the
295 fault surface, in Middle to Upper Jurassic strata (*Fig. 8c*). Throw decreases in all directions away from
296 the throw maximum and towards the tipline, although higher throw gradients are observed towards the
297 upper tip (*Fig. 8c*). This asymmetry is captured on a *T-z* plot taken from the centre of the fault that is
298 skewed towards the upper tip (*Fig. 7b*). There is minor thickening of the uppermost Jurassic and
299 Cretaceous succession in the hangingwall of the fault.

300 We interpret that the Rift Phase 2-related NW-SE-striking fault grew as an isolated structure
301 based on the lack of any evidence of mechanical interaction or linkage with any other faults, and the
302 gradual decrease in throw away from the centre of the fault surface (*Fig. 8*) (*cf.* Barnett et al., 1987;
303 Walsh and Watterson, 1989; Nicol et al., 1996). The position of maximum throw suggests that the
304 fault nucleated in Middle to Upper Jurassic stratigraphy (*Fig. 8b*). Thickening of strata across the fault
305 indicates that it was active and surface-breaking during the Late Jurassic and Cretaceous, an
306 interpretation supported by the flat upper tipline and high throw gradients near the upper tip, both of
307 which indicate that the upper tip was influenced by the free surface (*Figs. 5c, 7b and 8c*) (*cf.* Peacock
308 and Sanderson, 1991; Nicol et al., 1996; Childs et al, 2003; Baudon and Cartwright, 2008a, b and c).

309

310 ***5.2 Abutting Fault Interactions***

311 Fault F7 is a typical example of ‘Y-shaped’ intersection where one of the 2nd-stage NW-SE-striking
312 faults (F7), terminates (‘abuts’) against the Tusse Fault (*Figs. 4a, 9a-b*). Abutting interactions are the
313 most common linkage style along the Tusse Fault, occurring in both its hangingwall (e.g. Fault F4,
314 F14 and F16; *Fig 4a*) and footwall (e.g. Faults F5, F7 and F12; *Fig 4a*). Fault F7 lies in the footwall
315 of the Tusse Fault, is NE-dipping and terminates against a NE-SW-striking portion of the Tusse Fault
316 at branchline w-w’ (*Figs. 4a and 9*). The footwall block of F7 is shared with the footwall of the Tusse
317 Fault (*Fig. 9b*). Branchline w-w’ plunges gently towards the NNE and has a height of 1100 m (ca. 970
318 ms TWT), which approximates to the maximum height of Fault F7 (*Fig. 9b, d-e*). In contrast to the
319 isolated, non-interacting faults, the tipline of F7 is semi- rather than fully-elliptical due to the physical
320 link with the Tusse Fault (*cf. Figs. 8c and 9e*).

321 At the Top Sognefjord surface, throw on Fault F7 is highest at branchline w-w’ (ca. 90 m or
322 70 ms TWT) and decreases down to ca 30 m (23 ms TWT) 2.3 km away from the Tusse Fault (*Fig.*
323 *9c*). Along-strike of the Tusse Fault an abrupt southward increase in throw of ca. 90 m (70 ms TWT)
324 is observed across branchline w-w’ (*Fig. 9d*). The zone of higher throw corresponds with where the
325 footwall of the Tusse Fault also lies in the footwall of Fault F7 (*Fig. 9d*). The strike-projected throw
326 distribution on Fault F7 differs from that of isolated, non-interacting faults in two ways. Firstly, a

327 single throw maximum, centred on Middle to Upper Jurassic stratigraphy, is located immediately
328 adjacent to branchline w-w' rather than towards the centre of the fault, and secondly, throw contours
329 are semi- rather than fully-elliptical (*Fig. 9e*). From the throw maximum at the branchline, throw
330 decreases upwards, downwards and away from the branchline with the throw gradient being higher
331 towards the upper tipline (*Fig. 9e*).

332 Fault F7 is one of the NW-SE-striking set and, as such, was active only during Rift Phase 2,
333 as shown by the fault having a single throw maximum, and interpreted nucleation site, in post-RP1
334 Middle to Upper Jurassic stratigraphy. The location of the throw maximum on Fault F7 suggests the
335 abutting fault nucleated at, or within a few hundred metres of branchline w-w', with the unrestricted
336 lateral tip propagating SE into the footwall of the Tusse Fault and the other lateral tip being pinned by
337 the Tusse Fault. Thickening in the hangingwalls of the Tusse Fault and Fault F7, as well as higher
338 throw gradients towards their upper tips, indicates both faults were surface breaking during the Late
339 Jurassic and Early Cretaceous. As F7 abuts against the Tusse Fault, that is, the Tusse Fault restricted
340 the propagation of F7 into its hangingwall, it follows that F7 nucleated either at the same time or after
341 the reactivation of the Tusse Fault. We note that the 'step' in throw on the Tusse Fault across
342 branchline w-w' (*ca.* 90 m or 70 ms TWT) approximates the throw on Fault F7 near to the branchline
343 (*Figs 9c and d*). We suggest that the higher throw on the Tusse Fault to the south of the branchline is
344 due to the uplifted Tusse Fault footwall having received an 'extra' component of uplift from the
345 uplifted footwall of Fault F7 (i.e. local throw enhancement), whereas the lower throw to the north of
346 the branchline is due to the effect of uplift in the footwall of the Tusse Fault being counteracted by
347 subsidence of the hangingwall block of Fault F7 (i.e. local throw reduction).

348

349 ***5.3. Reactivated Relay Fault Interactions***

350 Reactivated relay interactions are rare along the Tusse Fault, with Fault F1 being the only example
351 (*Figs. 4a, 10a and b*). At this intersection the Tusse Fault consists of a *ca.* 1.1 km long, NW-SE-
352 striking, SW-dipping segment that links two major N-S-striking, W-dipping segments; based on this
353 geometric arrangement, we infer that the SW-dipping segment formed to accommodate breaching of a

354 relay zone developed between the two N-S-striking faults during Rift Phase 1 (*Figs. 10a and b*). This
355 short NW-SE-striking part of the Tusse Fault plane is composite or ‘shared’ with part of the linear
356 Fault F1, with portions of the F1 fault plane extending to the northwest and southeast of the composite
357 plane (*Figs. 10a and b*). Two southwesterly-plunging branchlines (x-x’ and y-y’) are developed on
358 Fault F1 and bound the composite fault plane (*Fig. 10*). Of these branchlines, x-x’ is located in the
359 northwest where the northern, N-S-striking part of the Tusse Fault intersects Fault F1, and y-y’ is
360 located in the southeast where the southern N-S-striking part of the Tusse Fault intersects Fault F1
361 (*Figs. 10b and d*). Portions of Fault F1 to the northwest and southeast of the composite fault plane,
362 respectively, are semi-elliptical and have lower tiplines residing in the uppermost Triassic succession
363 (*Fig. 10d*). However, the lower tipline of the composite fault plane, as with the Tusse Fault
364 elsewhere, extends down into the basement (*Fig. 10d*).

365 On a *T-x* plot at the Top Sognefjord structural surface (*Fig. 10c*), throw on Fault F1 increases
366 from zero at the lateral tips to 50-80 m (37-55 ms TWT) at the branchlines with the Tusse Fault. On
367 the N-S-striking components of the Tusse Fault, to the north and south of where its plane is shared
368 with Fault F1, throw values reach up to 380 m (260 ms TWT) (*Fig. 10c*). In contrast, along the NW-
369 SE-striking composite plane, composite throw values are higher 430-490 m (280-330 ms TWT) with
370 marked steps in throw coinciding with the locations of branchlines x-x’ and y-y’ (*Fig. 10c*), a trend
371 also shown on strike-projected throw plots (*Figs. 10d and e*). A *T-z* plot taken in the centre of the
372 composite fault reveals a throw profile typical of the Tusse Fault, with throw decreasing steadily
373 upwards in the Permian-Triassic and in the Upper Jurassic-to-Early Tertiary successions, and showing
374 no significant variation with depth in the intervening Jurassic succession (*Fig 7a*). The throw
375 distributions on portions of Fault F1 to the northwest and southeast of the composite plane, display
376 semi-elliptical throw contours, with each portion having a throw maximum located adjacent to the
377 composite plane and centred on Middle to Upper Jurassic stratigraphy (*Fig. 10d*). Throw decreases
378 away from the maxima near the branchlines in the same way as for abutting 2nd-stage faults, with the
379 throw gradients higher towards the upper rather than the lower tipline (cf. *Figs. 9e and 10d*).

380 We interpret that the composite fault and the N-S-striking segments of the Tusse Fault were both
381 active during Rift Phases 1 and 2 and buried and inactive during the Early to mid-Late Jurassic; this is

382 based on (i) the upward decrease in throw and the presence of growth beds in the Permian-Triassic
383 and Upper Jurassic-Lower Cretaceous successions; and (ii) consistent throws with depth in the
384 intervening Lower and Middle Jurassic successions (*Figs. 7a and 10e*). Given their similar growth
385 history but their differences in strike, we interpret that, by the end of Rift Phase 1, the NW-SE-
386 striking composite fault had breached a relay that separated the two N-S-striking segments, thus
387 linking the two. In contrast, the portions of Fault F1 lying to the northwest and southeast of the
388 composite segment were only active during Rift Phase 2, as indicated by the presence of Upper
389 Jurassic-Lower Cretaceous (but not Permian-Triassic) growth strata. Given that throw is highest on
390 the composite NW-SE-striking fault segment and that the throw maxima on portions of Fault F1
391 outside of the composite fault lie immediately adjacent to the branchlines with the Tusse Fault (*Figs.*
392 *10c-e*), we propose that, during Rift Phase 2, the NW-SE-striking portion of the Tusse Fault, which
393 previously represented a relay-breaching fault, was reactivated. This segment was exploited as a
394 nucleation site for Fault F1 prior to the fault propagating away to the NW and SE. As such, the NW-
395 SE-striking composite fault (the ‘reactivated relay-breaching fault’) accommodated throw that
396 accumulated on both the Tusse Fault and F1 during Rift Phase 2. We argue that the NW-SE-striking
397 ‘relay-breaching’ fault was exploited as nucleation site of 2nd stage faults during Rift Phase 2 due to it
398 being: i) preferentially oriented with respect to the new local, possibly NE-SW extension direction; or
399 ii) a releasing bend formed due to left-lateral oblique slip on the reactivated 1st-stage fault (*cf.* Morley
400 et al., 2004).

401 The interaction style described above shares some broad similarities with the ‘synthetic trailing
402 fault interaction’ described by Nixon et al. (2014). For example, both examples are associated with a
403 pre-existing (1st-stage) fault plane that displays locally high throw, bound by two branchlines
404 associated with hangingwall and footwall segments (*cf. Fig. 10* this study and *Figs 15 and 16* in
405 Nixon et al., 2014). However, a series of key geometric and kinematic observations suggest that the
406 style of interaction documented here is in fact different to that documented by Nixon et al. (2014) for
407 ‘synthetic trailing faults’. The most critical observation is that ‘synthetic trailing fault interactions’
408 form as two faults in the hangingwall and footwall of a pre-existing fault propagate towards, link with
409 (abut against), and eventually reactivate the pre-existing fault, thus resulting in a zone of locally high

410 throw and the formation of a connecting ‘trailing segment’ between the abutting faults. In contrast, in
411 the Horda Platform, it is the reactivated relay-breaching fault (or the ‘trailing segment’ of Nixon et al.,
412 2014) that reactivates first during the 2nd-stage of extension, propagating as a single fault into its
413 footwall and hangingwall. Given this fundamental kinematic difference, and that the dominant
414 influence on this interaction style is the reactivation of the relay-breaching fault inherited from Rift
415 Phase 1 and its continued propagation, we term this a ‘reactivated relay fault’ interaction style.

416

417 ***5.4. Hybrid and Retarding Fault Interactions***

418 Hybrid fault interactions are those that display evidence of more than one style of interaction or
419 linkage. Here we examine a particularly well-imaged example of a hybrid interaction that occurs
420 between the Tusse Fault and Fault F8. In plan view, at the Top Sognefjord structural surface, Fault F8
421 is linear and tips out *ca.* 200 m from the Tusse Fault (*Figs. 11a and b*). In the region between Fault F8
422 and the Tusse Fault a zone of intense ductile deformation is developed (*Figs. 4a, 11a and b*). In
423 contrast, at the Top Brent level, Fault F8 is hard-linked and abuts against the Tusse Fault at branchline
424 z-z’. Fault F8 downthrows to the SW, such that south of branchline z-z’ the hangingwall block is
425 shared with the Tusse Fault.

426 Away from the zone of ductile deformation (*ca.* 3 km from the Tusse Fault), the dip-oriented
427 geometry of Fault F8 is typical of that of the other NW-SE-striking faults (*Fig. 5c*). In cross-section
428 the upper tipline resides in the lowermost Tertiary interval and has a sub-horizontal morphology,
429 whereas the lower tipline, which is more poorly imaged, appears to be located in the Permian-Triassic
430 succession (*Figs. 5c and 11e*). Although the WNW tip of Fault F8 lies outside of the study area,
431 extrapolation of the tipline and strike-projected throw contours suggests the fault is semi-elliptical, a
432 function of having a branchline with the Tusse Fault (*Fig. 11e*). This branchline only extends for 50%
433 of the height of Fault F8, with the upper tip lying between the Top Brent and Top Sognefjord horizons
434 (*Fig. 11e*). The remaining upper section of Fault F8 does not share a branchline with the Tusse Fault
435 but instead is ‘soft-linked’ with the larger, pre-existing structure (*Fig. 11e*).

436 On a Top Sognefjord T - x plot, the projected throw (i.e. sum of brittle and ductile deformation)
437 of Fault F8 gradually increases towards the Tusse Fault (*Fig. 11c*). In contrast, true throw (solely
438 brittle deformation) gradually increases up to a point ca. 1.3 km from the Tusse Fault before sharply
439 decreasing to zero ca. 200 m from the Tusse Fault (*Fig. 11c*). A Top Sognefjord T - x plot along-strike
440 of the Tusse Fault (*Fig. 11d*) highlights an abrupt southwards increase, a near doubling, of throw
441 across the branchline with F8, that is, the transition from where the hangingwall of the Tusse Fault is
442 associated with the footwall of F8 to the portion where the hangingwall of the Tusse Fault and the
443 hangingwall of F8 are shared (*Figs. 4b and 11d*). Furthermore, *Fig. 11c* illustrates striking variations
444 in how throw is partitioned between ductile and brittle components across the intersection. First, the
445 summed amplitude of folding associated with F8 (grey shading) increases from ca. 25 m (ca. 20 ms
446 TWT) approximately 1.3 km from the Tusse Fault to 320 m (ca. 220 ms TWT) at the intersection with
447 the Tusse Fault (*Fig. 11c*). Second, the T - x plot along the Tusse Fault reveals a significant increase in
448 the summed amplitude of folding from 0 m to ca. 300 m moving southwards across the branchline
449 with F8 (*Fig. 4b*).

450 The throw distribution on Fault F8 shows a single maximum that is centred on Mid-to-Upper
451 Jurassic stratigraphy (*Fig. 11e*) and is neither located in the centre of the fault, as with isolated, non-
452 interacting faults, or immediately adjacent to the branchline with the Tusse Fault, as with abutting
453 faults (*cf. Figs 8c and 9e*). Instead, the throw maximum is lobate in shape and, although throw is high
454 near the branchline, the maximum throw is centred ca. 1.3 km into the hangingwall of the Tusse Fault
455 (*Fig 11e*). Throw smoothly decreases away from throw maximum in all directions such that throw
456 contours near the branchline are horizontal (*Fig. 11e*).

457 The location of the true throw maximum leads us to interpret that F8 nucleated ca. 1.3 km into the
458 hangingwall of the Tusse Fault in the Mid-to Late Jurassic succession before propagating to the
459 WNW and ESE. It is likely that, as the ESE tip of Fault F8 approached the Tusse Fault, the relative
460 dips of Tusse Fault and Fault F8, in combination with the tipline geometry of Fault F8 meant that the
461 Fault F8 only abutted against, and locally linked with the Tusse Fault along a short branchline and at
462 relatively deep structural levels (i.e. below the Top Sognefjord horizon) (*Fig. 11e*). In contrast, at and
463 above the Top Sognefjord horizon, Fault F8 did not abut against, or develop a branchline with the

464 Tusse Fault (*Figs. 11a, b, c and e*). Instead, we interpret that the combination of the intense ductile
465 deformation ahead of the ESE tip of Fault F8 at shallow levels, the skew of true throw on Fault F8
466 towards the Tusse Fault and the high throw gradient near the branchline indicate that ESE-directed tip
467 propagation in the shallow portion was mechanically retarded by the Tusse Fault (*cf.* Manighetti et al.,
468 2001; Nelson, 2006; Nixon et al., 2014). Despite the lack of hard-linkage between the Tusse Fault and
469 Fault F8 at the Top Sognefjord level and above, when projected throw (i.e. that which sums ductile
470 and brittle deformation) is used to determine a Top Sognefjord *T-x* profile along the Tusse Fault, the
471 ductile deformation ahead of the ESE tip of Fault F8 ensures that a ‘step’ increase in throw towards
472 the shared hangingwall block (*Fig. 11d*). Given that Fault F8 shows evidence of both abutting against,
473 and being mechanically retarded by the Tusse Fault, this example has effectively been fossilised
474 during the transition from one interaction style to another, capturing two discrete stages in the
475 evolutionary sequence of fault intersections.

476

477 **6. Discussion**

478

479 ***6.1. Styles of Fault Interaction and Linkage in Multiphase Rifts***

480 In this study, 2nd-stage faults interact with the reactivated Tusse Fault to varying extents; some faults
481 are physically and kinematically isolated from the larger structure (*ca.* 60%), some abut against it (*ca.*
482 30%) or show evidence of having been retarded by it, whereas others exploit and reactivate earlier
483 relay zones (*Figs. 4a, 8-11*). The fault interactions observed from a natural multiphase system in this
484 study are supported by findings from physical models as well as other natural systems (e.g. Bonini et
485 al., 1997; Keep and McClay, 1997; Bellahsen et al., 2005; Henza et al., 2010; 2011). First, we note
486 that reactivation of 1st-stage faults is broadly synchronous with the nucleation of 2nd-stage faults, a
487 characteristic observed in physical models specifically created to investigate how the growth of 2nd-
488 stage faults is influenced by the number and maturity of 1st-stage faults and changes in extension
489 direction (<45°) (Henza et al. 2010; 2011). Second, our observation that some of the 2nd-stage faults

490 nucleated at reactivated 1st-stage faults, is supported by a range of studies which suggest that pre-
491 existing faults can act as nucleation sites for 2nd-stage faults (*Figs. 8-12*) (e.g. Meyer et al., 2002;
492 Walsh et al., 2002; Henza et al., 2010; 2011). Third, we observe 2nd-stage faults that abut against, or
493 show evidence of having been retarded by the reactivated 1st-stage fault (e.g. F6-F8 and F12-F14;
494 *Fig. 4a*) and some that curve into parallelism with the main structure when in close proximity (e.g.
495 F15; *Fig. 4a*). These observations suggest the Tusse Fault has acted as mechanical barrier and
496 perturbed the regional stress field, thus restricting and influencing the propagation of later faults (*cf.*
497 Færseth et al., 1997; Færseth and Ravnås, 1998; Bellahsen et al., 2005; Nelson, 2006; Henza et al.,
498 2011; Nixon et al., 2014).

499 Although there are similarities between the fault interactions in this study and those described
500 from physical modelling studies and other natural fault systems, there are also some differences. In
501 particular, in models D and E in Henza et al. (2011), where 1st-stage faults are well-developed before
502 the extension direction changes for the second rift phase, a high number of 2nd-stage faults cross-cut
503 1st-stage faults. However, we see no evidence of 2nd-stage faults cutting across and offsetting the
504 Tusse Fault (*e.g. Fig 4a*), which may be due to the restricted sample size of fault interactions in this
505 study relative to that in the models of Henza et al. (2011). Another potential cause for the absence of
506 cross-cutting interactions may be that, in our natural example, fault interactions were catalogued on
507 the Top Sognefjord surface, an essentially ‘intra-rift’ surface (i.e. deposited between Rift Phase 1 and
508 2). In contrast, in the models of Henza et al. (2011), syn-rift layers were not added during either phase
509 of extension, and hence fault interactions were catalogued on a true pre-rift surface. As such, the
510 reactivated Tusse Fault had to propagate upwards through overlying intra-rift sediments, potentially
511 reducing the opportunity for 2nd-stage faults to cross-cut it.

512 Based on map view geometry alone (*Figs. 10a and b*), the reactivated relay fault interaction
513 could be mistaken for a simple cross-cutting fault relationship. However, kinematic analysis reveals
514 that, during Rift Phase 2, the NW-SE-striking relay-breaching fault developed in Rift Phase 1 was
515 reactivated and exploited as a nucleation site for NW-SE-striking Fault F1, which propagated to the
516 NW and SE, away from the ‘composite’ fault plane (*Fig. 10*). We demonstrate that the 1st- and 2nd-

517 stage faults at the reactivated relay fault interaction were then active synchronously during Rift Phase
518 2, such that the relay fault became a ‘zone of shared throw’.

519 Given that the Tusse Fault was fully reactivated during Rift Phase 2, we do not document
520 2nd-stage faults cross-cutting and offsetting *inactive* 1st-stage structures (*sensu* Needham et al.,
521 1996). Such interactions will be more common in multiphase rifts where the extension directions
522 between the two rift phases are highly oblique ($>45^\circ$), such that reactivation of 1st-stage faults is not
523 favoured (e.g. Nelson, 2006). We also speculate that, in general, a higher frequency of fault bends and
524 relay-breaching faults along 1st-stage faults, in combination with a favourable extension direction in
525 the second phase of extension, may result in more potential nucleation sites for 2nd-stage faults (*cf.*
526 Lezzar et al., 2002; Bellahsen et al, 2005; 2006).

527

528 ***6.2. The Geometry and Throw Patterns of Faults in Multiphase Rifts***

529 We have documented the styles of interaction that occur between non-colinear faults in a multiphase
530 fault network. In particular, we have demonstrated that a wide range of interaction styles and patterns
531 of throw develop in association with non-colinear faults, with the key relationships synthesised in
532 *Figure 12*. The tipline geometries of 2nd-stage, non-colinear faults that interact with 1st-stage faults
533 may vary depending on the interaction style and whether the faults are blind or surface-breaking (*Fig.*
534 *12*). Flat upper tiplines are typically associated with surface-breaking faults and convex-upward upper
535 tiplines are associated with blind faults (*Fig. 12*) (e.g. Nicol et al., 1996; Childs et al. 2003; Baudon
536 and Cartwright, 2008). In the simplest scenario in which faults are blind, where a 2nd-stage fault
537 nucleates and propagates in isolation from a 1st-stage fault, both faults will tend towards having
538 elliptical tiplines (*Fig. 12a*). In the case that both faults are free from lithological restriction, both
539 faults should theoretically tend towards an aspect ratio of 2 (e.g. Nicol et al., 1996). In contrast, where
540 a 2nd-stage fault is laterally restricted by a pre-existing fault (*Figs. 12b and c*), the geometry of the
541 2nd-stage fault tipline can be highly variable, although typically more asymmetric in form and, in the
542 case that the faults are blind, should have an aspect ratio <2 . In cases where a 2nd-stage fault

543 nucleates at a pre-existing fault, the tipline geometry of the 2nd-stage fault will be semi-elliptical, due
544 to the physical link with the pre-existing fault (*Figs. 12d and e*).

545 If we consider the characteristics of a 2D *T-x* profile taken along-strike of a reactivated 1st-
546 stage fault (e.g. *Fig. 4b*), it can be seen that throw does not vary smoothly across the fault surface;
547 rather, it is characterised by ‘steps’ in throw where the Tusse Fault is influenced by physical or
548 kinematic interactions with 2nd-stage faults. Thus, *T-x* profiles along reactivated structures that are
549 hard or soft-linked to newly-formed faults will differ from those from faults developed in response to
550 the growth of a single fault segment (*cf.* Watterson, 1986; Barnett et al., 1987; Nicol et al., 1996;
551 Needham et al., 1996) or the linkage of smaller precursor segments (*cf.* Anders and Schlische, 1994;
552 McLeod et al., 2000; Young et al., 2001). We also note how the magnitude of ductile deformation
553 along-strike of a reactivated 1st-stage fault also displays ‘steps’ in the profile, correlating with
554 locations where 2nd-stage faults soft or hard-link with the 1st-stage fault (*Fig. 4b*). Furthermore, the
555 way in which throw is partitioned between interacting faults and across branchlines is dependent on
556 the interaction style (*Figs. 8-12*). For example, where a 2nd-stage fault is isolated from, and not
557 laterally restricted by a 1st-stage fault, the throw maximum on the 2nd-stage fault is located towards
558 the fault centre, with throw decreasing smoothly and linearly towards the tips (*Figs. 8 and 12a*).
559 Where a 2nd-stage fault nucleates at and propagates away from a pre-existing structure, either into its
560 hanging-wall or footwall, the mutual hanging-wall or footwall block experiences an additional
561 component of subsidence or uplift, respectively (*Figs. 9, 12d and e*). On the 1st-stage fault, this is
562 expressed by a sharp increase in the throw towards the shared hangingwall or footwall block (*Figs.*
563 *12d and e*) (*sensu* Nelson, 2006; Nixon et al., 2014). The 2nd-stage fault will be bound by a steep
564 branchline, along which the maximum throw occurs such that throw contours are semi-elliptical (*Figs.*
565 *12d and e*). In cases where the 2nd-stage fault grows towards and is retarded by the 1st-stage fault, the
566 throw maximum on the 2nd-stage fault will be located towards the laterally-restricted portion of the
567 fault, with high throw gradients developing near the restricted tip (*Fig. 12b*) (*sensu* Manighetti et al.,
568 2001; Nixon et al. 2014).

569 The individual styles of fault interaction and linkage captured in this study, and those of
570 Nixon et al. (2014), show discrete stages of interaction development. However, observations from

571 physical modelling studies (e.g. Henza et al., 2010; 2011) indicate that fault intersection development
572 is a dynamic process, involving a gradual transition from one style to another. For example, 2nd-stage
573 faults which nucleate away from 1st-stage faults and grow initially as isolated 2nd-stage faults (e.g.
574 *Figs. 8 and 12a*), may propagate towards and be retarded by the 1st-stage fault resulting in higher
575 throw gradients towards the retarded tip (e.g. *Figs. 11 and 12b*) (*sensu* Manighetti et al., 2001; Nixon
576 et al. 2014) prior to hard-linking with, and abutting against, the 1st-stage fault (e.g. *Figs. 9 and 12c*)
577 (see also Nelson et al., 2006). This study suggests that abutting faults are unlikely to evolve to cross-
578 cut the earlier fault; in this study, cross-cutting is restricted to a breached fault segment boundary
579 along-strike of the Tusse Fault (cf. Nelson, 2006). In contrast, in the case of 2nd-stage faults that
580 nucleate at and propagate away from 1st-stage faults (*Figs. 12d and e*), the branchline will be formed
581 relatively early, and the style of interaction at the abutting tip would not change once the full
582 branchline is developed.

583

584 ***6.3. Implications for the Evolution of Multiphase Rift Fault Networks***

585 In the Northern Horda Platform both N-S- and NW-SE-striking faults were active synchronously
586 during Rift Phase 2, even at complex intersections. It is thus likely that at least one, or possibly both,
587 of these fault sets experienced oblique slip. Our simplest and preferred explanation is that, at least
588 locally within the study area, the extension direction during Rift Phase 2 was reoriented to be NE-SW,
589 sub-perpendicular to the strike of the majority of the NW-SE-striking faults; if true, this implies that
590 the N-S-striking Tusse Fault may have been reactivated obliquely with a left-lateral sense of slip. The
591 strike-parallel component of any oblique slip is likely to have been fairly low as no strong evidence of
592 flower structures or laterally offset markers is noted in the 3D volume. In contrast, the observation of
593 growth strata and vertical fault throw for the vast majority of faults in the array is evidence for a
594 significant amount of fault activity with a dip-slip component.

595 We have developed a conceptual model highlighting the key characteristics of multiphase rift
596 fault networks, drawing on observations from the northern Horda Platform, other natural rift fault
597 networks, and physical models (*Fig. 13*). By comparing figures 1 and 13, the significant differences

598 between non-colinear fault networks developed during single-phase and multiphase extension become
599 clear. For example, non-colinear faults are more pervasive in a multiphase network than would
600 typically occur in a single-phase rift, and multiphase rift fault networks are more complex and
601 connected, being influenced by a larger number of fault interactions and wider range of interaction or
602 linkage styles (*cf.* Figs 1 and 13). However, we can also see how individual non-colinear fault
603 relationships developed in single- and multiphase rift networks can appear geometrically similar (*cf.*
604 Figs 1 and 13). For example, abutting faults developed during a second phase of extension are, when
605 viewed individually, indistinguishable from splay faults and release faults developed during a single
606 rift phase; all strike oblique to the main fault and tend to have a nucleation site and throw maximum
607 near the main fault (e.g. Baudon et al., 2008a; Nixon et al. 2014) (*cf.* Figs 1 and 13). We suggest that,
608 determining the origin of non-colinear faults requires knowledge of the relative timing of fault
609 activity. In natural fault networks, this knowledge is best gained by studying data-rich areas where
610 borehole-constrained 3D seismic data allows constraints to be placed on the age of growth strata
611 adjacent to the faults. If the non-colinear fault in question is an abutting fault developed during a
612 second rift phase rather than a splay fault developed during a single rift phase, activity on this fault
613 should correspond to the second rift phase and hence post-date the initial activity on the main fault. In
614 addition to determining the relative timing of fault activity, the location of the interaction with regards
615 to the tips and segment centres of 1st-stage faults and/or the relative abundance of the interaction type
616 within the network can also help distinguish between different causal mechanisms. For example: i)
617 relatively small splay faults will likely cluster at the tips of the main faults; ii) release faults will tend
618 to be located at sites of throw maxima and minima along-strike of the main faults; and iii) abutting
619 faults developed due to a second phase of extension will be part of a pervasive non-colinear array (e.g.
620 Reeve et al., 2015).

621 Overall, the approach to the analysis of fault interactions applied in this study and the key
622 findings are applicable to any rift setting characterised by dip-slip non-colinear faults. We present new
623 insights into the geometries, throw patterns and kinematics of faults associated with different fault
624 interaction styles in a multiphase rift, providing a basis for future studies examining the how single-
625 phase and multiphase rift fault networks evolve.

626

627 7. Conclusions

628

629 Analysis of a 3D borehole-constrained seismic dataset from the northern Horda Platform reveals a
630 network of non-colinear faults that developed due to multiple phases of extension. The fault network
631 consists of a high-throw N-S-striking fault which was active during Rift Phases 1 and 2 and a series of
632 shorter, NW-SE-striking faults which were only active during Rift Phase 2. We show that:

633

- 634 1. In the northern Horda Platform fault network, a multiphase network that experienced a
635 different local extension direction in each rift phase, non-colinear faults are more pervasive
636 than in networks developed during a single phase of extension. Furthermore, the northern
637 Horda Platform network is more complex and connected than a typical single-phase network,
638 being influenced by a higher frequency of interactions between 1st and 2nd-stage faults.
- 639 2. A wide range of styles of fault interaction can occur between 1st- and 2nd-stage faults in
640 multiphase rift fault networks that have experienced a different local extension direction in
641 each phase. At the Top Sognefjord structural level in the northern Horda Platform network we
642 document 2nd-stage faults that are isolated from the 1st-stage fault (*ca.* 60%), abut against it
643 (*ca.* 30%), or those that exploit breached relay zones along the Tusse Fault or show evidence
644 of the propagation of the fault having been retarded by it (*ca.* 10% combined).
- 645 3. In multiphase rift fault networks, the typical geometries of fault tiplines and the distribution of
646 throw on fault surfaces are highly-variable, being controlled to a large extent by the style of
647 interaction between 1st-stage and 2nd-stage faults. In particular we note how: i) the tiplines of
648 many 2nd-stage faults are semi-elliptical due to the development of branchlines at sites of
649 intersection with 1st-stage faults; ii) the distribution of throw on reactivated 1st-stage faults
650 will be modified in a predictable manner if they are intersected or influenced by 2nd-stage
651 faults; iii) pre-existing faults can act as sites of nucleation for 2nd-stage faults as well as
652 mechanical barriers that restrict or alter the propagation pathways of 2nd-stage faults; and iv)

653 fault segment boundaries, and fault kinks or corrugations along first-stage faults, can act as
654 preferential nucleation sites for 2nd-stage faults.

655 4. The observation of a 2nd-stage fault that shows evidence of concurrently abutting against, and
656 being mechanically retarded by a 1st-stage fault indicates fault interactions are not static and
657 transition from one style to another. For example, 2nd-stage faults that nucleate away from,
658 and propagate towards a 1st-stage fault may initially be isolated, before being mechanically
659 retarded by, and eventually abutting and hard-linking with the 1st-stage fault.

660

661 Overall, we highlight how it is important to integrate borehole-constrained 3D seismic data with a
662 systematic approach to the analysis of fault geometry and throw distributions in a fault network. This
663 approach will allow interpreters greater confidence in mapping fault intersections in seismic datasets
664 that lack clear imaging of faults and their geometric relationships, as well as in determining whether
665 non-colinear fault networks developed during single- or multiple phases of rifting.

666

667 **8. Acknowledgements**

668 We thank Craig Magee, Casey Nixon, Atle Rotevatn and Haakon Fossen for constructive discussions
669 during this project, and Alissa Henza and an anonymous reviewer for constructive reviews. We thank
670 Nancy Cottington for help with figure editing. Schlumberger are thanked for providing an academic
671 license for Petrel. This contribution forms part of the MultiRift Project funded by the Research
672 Council of Norway (Project number 215591/E30) and Statoil to the University of Bergen and partners
673 Imperial College, University of Manchester and University of Oslo. We also thank Statoil and NPD
674 for providing access to seismic and well data. Statoil are thanked for permission to publish the results
675 of this study. Conclusions from this paper do not necessarily reflect the views of Statoil or partners.

676

677 **9. Figure Captions**

678 **Figure 1:** Block model showing simple large-scale co-linear faults developed during a single-phase of
679 rifting as well as the typical locations of any non-colinear faults that may develop (RP1 = rift phase 1,
680 arrows indicate extension direction)

681 **Figure 2:** (a) Principal tectonic structures of the northern North Sea, after Færseth (1996) and Bell et
682 al., (2014). The Horda Platform (HP), the focus of this study is outlined in red and the location of the
683 regional interpretation shown in Figure 1c is shown by a bold black line. (b) Map showing the non-
684 colinear fault sets in the northern Horda Platform fault array, colour-coded to highlight which faults

685 were active in Rift Phase 1 (Permian-Triassic) and Rift Phase 2 (Late Jurassic – Cretaceous) (after
686 Whipp et al., (2014)). (c) Regional interpretation of the structure of the northern North Sea after
687 Færseth (1996).

688 **Figure 3:** Stratigraphic framework with a synthetic seismogram for well 31/6-6, showing the ages
689 and representative lithologies of the key Groups and Formations in the Horda Platform along with key
690 seismic stratigraphic markers (after Faerseth (1996) and Whipp et al., (2014) and modified from Bell
691 et al., (2014)). Tectonic events based on the timing of activity of the Tusse Fault and nearby structures
692 (after Whipp et al.,2014). A representative section of seismic reflection data from a 2D survey is
693 shown to illustrate the typical seismic stratigraphy in the area. Colour coding of the seismic
694 stratigraphic marker horizons and megasequences is continued throughout. P=Period and E=Epoch.
695 TD = Growth and deflation of the central North Sea thermal dome. *The timing of the initiation and
696 cessation of Syn-Rift Phase 2 is diachronous across the Horda Platform (see Bell et al., 2014 for more
697 details).

698
699 **Figure 4:** (a) TWT structure map of Top Sognefjord Fm with key faults labelled. (b) $T-x$ plot and
700 distribution of ductile deformation (summed fold amplitudes) along-strike of the Tusse Fault system.
701 Note the ‘steps’ in throw at sites of interaction with NW-SE-striking faults and how throw and degree
702 of ductile deformation correlate along-strike of the Tusse Fault.

703 **Figure 5:** Series of seismic profiles and geoseismic sections illustrating key structural characteristics
704 of the Tusse Fault system and the NW-SE-striking faults (locations of sections shown in Fig. 4a). (a)
705 Seismic section and geoseismic section oriented orthogonal to the Tusse Fault system in the south of
706 the study area. (b) Seismic section and geoseismic section oriented orthogonal to the Tusse Fault
707 system in the north of the study area. (c) Seismic section and geoseismic section oriented orthogonal
708 to a series of NW-SE-striking faults in the study area.

709 **Figure 6:** TWT-thickness maps for a series of stratigraphic intervals: (a) Permian-Triassic (Rift Phase
710 1), (b) Lower Jurassic to mid Upper Jurassic (intra-rift cessation) and (c) mid Upper Jurassic and
711 Cretaceous (Rift Phase 2). Note how thickening across the Tusse Fault is observed only in (a) and (c).

712 **Figure 7:** (a) $T-z$ plots taken at various locations along the N-S-striking Tusse Fault and b) $T-z$ plots
713 taken from various NW-SE-striking faults. Note that the locations of the plots in a) and b) are marked
714 by stars on Fig 4a. These plots provide evidence that the Tusse Fault was active during Rift Phases 1
715 and 2 whereas NW-SE-striking faults only initiated during Rift Phase 2 (see text for more details).

716 **Figure 8:** Quantitative analysis of the isolated, non-interacting NW-SE-striking Fault F11. (a)
717 Oblique view at the Top Sognefjord structural surface, image taken looking SE (V.E x5). (b) $T-x$
718 profile along Fault F11 at the Top Triassic and Top Sognefjord structural surfaces, with the highest
719 throw located towards the centre of Fault F11. (c) Strike-projected throw distribution in ms TWT of
720 Fault F11 with no vertical exaggeration. A single throw maximum is located towards the upper centre
721 of the fault and throw contours are broadly elliptical. Projected fault cut-offs of key seismic
722 stratigraphic horizons are shown with solid lines marking hanging-wall cut-offs and dashed lines
723 footwall cut-offs (continued in Figures 9-11).

724 **Figure 9:** Quantitative analysis of the ‘abutting’ interaction between the Tusse Fault and Fault F7. (a)
725 plan and (b) oblique views of the interaction at the Top Sognefjord structural surface (V.E x5). (c) $T-x$
726 profile along Fault F7 at the Top Sognefjord horizon. (d) N-S $T-x$ profile along the Tusse Fault near
727 branchline w-w’ with Fault F7 at the Top Sognefjord horizon. Note the step-like increase in throw
728 immediately south of branchline w-w’ in the region of the mutual footwall. Strike-projected throw
729 distribution in ms TWT on abutting Fault F7 with no vertical exaggeration. The tipline and throw
730 contours are semi-elliptical with a single maximum located near the branchline.

731 **Figure 10:** Quantitative analysis of the reactivated relay interaction between the Tusse Fault and Fault
732 F1. (a) Plan and (b) oblique views of the intersection at the Top Sognefjord horizon (V.E x5). (c) $T-x$
733 profile along both faults at the Top Sognefjord structural surface. Note the higher throw between

734 branchlines x-x' and y-y' in the portion of the fault plane that is shared with the Tusse Fault. (d)
735 Strike-projected throw distribution in ms TWT of Fault F1 with no vertical exaggeration. The highest
736 throw is located between branchlines x-x' and y-y'. On the portions of Fault F1 either side of
737 branchlines x-x' and y-y', fault throw are highest nearer the branchline and throw contours are semi-
738 elliptical. (e) Strike-projected throw distribution in ms TWT of the Tusse Fault with no vertical
739 exaggeration. Throw is highest between branchlines x-x' and y-y'.

740 **Figure 11:** Quantitative analysis of the interaction between the Tusse Fault and Fault F8, a 'hybrid'
741 interaction that shows evidence of both abutment and retardation. (a) plan and (b) oblique views of the
742 intersection at the Top Sognefjord horizon (V.E x5). (c) *T-x* profile showing true throw along Fault F8
743 at the Top Brent horizon and both the true throw and projected throw along Fault F8 at the Top
744 Sognefjord horizon; the true throw at the Top Sognefjord horizon is skewed towards the Tusse Fault
745 suggesting the Tusse Fault has retarded the propagation of F8. (d) N-S *T-x* profile showing projected
746 throw at the Top Sognefjord structural surface along the Tusse Fault near 'apparent' branchline z-z'
747 with F8. Note the step-like increase in throw immediately south of the 'apparent' branchline z-z' in
748 the region of the mutual hangingwall block. Strike-projected throw distribution in ms TWT of Fault
749 F8 with no vertical exaggeration. Note: i) the short branchline that marks the abutment of F8 against
750 the Tusse Fault; and ii) the area above the short branchline marked by ductile deformation is
751 interpreted to represent 'retardation' of Fault F8 by the Tusse Fault.

752 **Figure 12:** Conceptual models showing how different fault interaction styles influence fault tipline
753 geometry and throw patterns in multiphase rifts. Colour-coding of throw projections: purple
754 represents lowest throw; blue, yellow and orange represent increasing respective throw amounts and
755 red represents the highest throw.

756 **Figure 13:** Conceptual model fault network in a multiphase rift showing typical locations of, and
757 styles of interaction between non-colinear faults. The model assumes that the extension direction in
758 Rift Phases 1 and 2 are different and that faults developed in Rift Phase 1 are reactivated during Rift
759 Phase 2. (RP1 = rift phase 1, resulting in the formation of faults outlined in red; RP2 =Rift Phase 2,
760 resulting in faults outlined in blue).

761 **Appendix 1** – Time-depth plots for seven key wells in close proximity to the Tusse Fault and a best-
762 fit trendline which was used for depth conversion.

763

764 10. References

765 Aydin, A., Reches, Z.E., 1982. Number and orientation of fault sets in the field and in experiments. *Geology* 10,
766 107-112.

767

768 Bailey, W., Walsh, J., Manzocchi, T., 2005. Fault populations, strain distribution and basement fault reactivation in
769 the East Pennines Coalfield, UK. *Journal of Structural Geology* 27, 913-928.

770

771 Barnett, J.A., Mortimer, J., Rippon, J.H., Walsh, J.J., Watterson, J., 1987. Displacement geometry in the volume
772 containing a single normal fault. *AAPG Bulletin* 71, 925-937.

773

774 Bartholomew, I., Peters, J., Powell, C., 1993. Regional structural evolution of the North Sea: oblique slip and the
775 reactivation of basement lineaments, Geological Society, London, Petroleum Geology Conference series.
776 Geological Society of London 4, 1109-1122.

777

778 Baudon, C., Cartwright, J., 2008a. Early stage evolution of growth faults: 3D seismic insights from the Levant Basin,
779 Eastern Mediterranean. *Journal of Structural Geology* 30, 888-898.

780

781 Baudon, C., Cartwright, J., 2008b. The kinematics of reactivation of normal faults using high resolution throw
782 mapping. *Journal of Structural Geology* 30, 1072-1084.

783
784 Baudon, C., Cartwright, J.A., 2008c. 3D seismic characterisation of an array of blind normal faults in the Levant
785 Basin, Eastern Mediterranean. *Journal of Structural Geology* 30, 746-760.
786
787 Bell, R.E., Jackson, C.A.L., Whipp, P.S., Clements, B., 2014. Strain migration during multiphase extension:
788 Observations from the northern North Sea. *Tectonics*. 33, 1936-1963.
789
790 Bellahsen, N., Daniel, J.M., 2005. Fault reactivation control on normal fault growth: an experimental study. *Journal*
791 *of Structural Geology* 27, 769-780.
792
793 Bellahsen, N., Fournier, M., d'Acremont, E., Leroy, S., Daniel, J., 2006. Fault reactivation and rift localization:
794 Northeastern Gulf of Aden margin. *Tectonics* 25, TC1007.
795
796 Bonini, M., Souriot, T., Boccaletti, M., Brun, J.P., 1997. Successive orthogonal and oblique extension episodes in a
797 rift zone: Laboratory experiments with application to the Ethiopian Rift. *Tectonics* 16, 347-362.
798
799 Brun, J.-P., Tron, V., 1993. Development of the North Viking Graben: inferences from laboratory modelling.
800 *Sedimentary Geology* 86, 31-51.
801
802 Burgmann, R., Pollard, D.D., Martel, S.J., 1994. Slip distributions on faults: effects of stress gradients, inelastic
803 deformation, heterogeneous host-rock stiffness, and fault interaction. *Journal of Structural Geology* 16, 1675-
804 1690.
805
806 Cartwright, J.A., Lonergan, L., 1996. Volumetric contraction during the compaction of mudrocks: A mechanism for
807 the development of regional-scale polygonal fault systems. *Basin Research* 8, 183-193.
808
809 Cartwright, J.A., Dewhurst, D., 1998. Layer-bound compaction faults in fine-grained sediments." *Geological Society*
810 *of America Bulletin* 110(10): 1242-1257.
811
812 Cartwright, J.A., Mansfield, C.S., 1998. Lateral displacement variation and lateral tip geometry of normal faults in
813 the Canyonlands National Park, Utah. *Journal of Structural Geology* 20, 3-19.
814
815 Cartwright, J.A., Trudgill, B.D., Mansfield, C.S., 1995. Fault growth by segment linkage: an explanation for scatter in
816 maximum displacement and trace length data from the Canyonlands Grabens of SE Utah. *Journal of Structural*
817 *Geology* 17, 1319-1326.
818
819 Chapman, T., Meneilly, A., 1991. The displacement patterns associated with a reverse-reactivated, normal growth
820 fault. *Geological Society, London, Special Publications* 56, 183-191.
821
822 Chattopadhyay, A., Chakra, M., 2012. Influence of pre-existing pervasive fabrics on fault patterns during
823 orthogonal and oblique rifting: An experimental approach. *Marine and Petroleum Geology*.
824
825 Childs, C., Nicol, A., Walsh, J.J., Watterson, J., 2003. The growth and propagation of synsedimentary faults. *Journal*
826 *of Structural Geology* 25, 633-648.
827
828 Conneally, J., Childs, C., and Walsh, J.J., 2014. Contrasting origins of breached relay zone geometries. *Journal of*
829 *Structural Geology* 58, 59-68.
830
831 Corti, G., 2004. Centrifuge modelling of the influence of crustal fabrics on the development of transfer zones:
832 Insights into the mechanics of continental rifting architecture. *Tectonophysics* 384, 191-208.
833
834 Corti, G., van Wijk, J., Cloetingh, S., Morley, C.K., 2007. Tectonic inheritance and continental rift architecture:
835 Numerical and analogue models of the East African Rift system. *Tectonics* 26.
836
837 Coward, M., Dewey, J., Hempton, M., Holroyd, J., 2003. Tectonic evolution. *The millennium atlas: Petroleum*
838 *geology of the central and northern North Sea*, 17-33.
839

840 Cowie, P.A., Underhill, J.R., Behn, M.D., Lin, J., Gill, C.E., 2005. Spatio-temporal evolution of strain accumulation
841 derived from multi-scale observations of Late Jurassic rifting in the northern North Sea: A critical test of models
842 for lithospheric extension. *Earth and Planetary Science Letters* 234, 401-419.
843

844 Davies, R., Turner, J., Underhill, J., 2001. Sequential dip-slip fault movement during rifting: a new model for the
845 evolution of the Jurassic trilete North Sea rift system. *Petroleum Geoscience* 7, 371-388.
846

847 Dawers, N.H., Underhill, J.R., 2000. The role of fault interaction and linkage in controlling synrift stratigraphic
848 sequences: late Jurassic, Statfjord East Area, northern North Sea. *AAPG Bulletin* 84, 45.
849

850 Destro, N., 1995. Release fault: A variety of cross fault in linked extensional fault systems, in the Sergipe-Alagoas
851 Basin, NE Brazil. *Journal of Structural Geology* 17, 615-629.
852

853 Doré, A., Lundin, E., Fichler, C., Olesen, O., 1997. Patterns of basement structure and reactivation along the NE
854 Atlantic margin. *Journal of the Geological Society* 154, 85-92.
855

856 Dreyer, T., Whitaker, M., Dexter, J., Flesche, H., Larsen, E., 2005. From spit system to tide-dominated delta:
857 integrated reservoir model of the Upper Jurassic Sognefjord Formation on the Troll West Field, Geological
858 Society, London, *Petroleum Geology Conference series*. Geological Society of London, pp. 423-448.
859

860 Færseth, R., 1996. Interaction of Permo-Triassic and Jurassic extensional fault-blocks during the development of
861 the northern North Sea. *Journal of the Geological Society* 153, 931-944.
862

863 Færseth, R.B., Ravnås, R., 1998. Evolution of the Oseberg Fault-Block in context of the northern North Sea
864 structural framework. *Marine and Petroleum Geology* 15, 467-490.
865

866 Fossen, H., 1992. The role of extensional tectonics in the Caledonides of south Norway. *Journal of structural
867 geology* 14, 1033-1046.
868

869 Gawthorpe, R., Leeder, M., 2000. Tectono-sedimentary evolution of active extensional basins. *Basin Research* 12,
870 195-218.
871

872 Glennie, K.W. (1987). Outline of North Sea History and structural framework. In: *Introduction to the Petroleum
873 Geology of the North Sea*. 3rd Edition. Blackwell Scientific Publications, Oxford 34-77
874

875 Helland-Hansen, W., Ashton, M., Lømo, L., Steel, R., 1992. Advance and retreat of the Brent delta: recent
876 contributions to the depositional model. *Geological Society, London, Special Publications* 61, 109-127.
877

878 Henza, A.A., Withjack, M.O., Schlische, R.W., 2010. Normal-fault development during two phases of non-coaxial
879 extension: An experimental study. *Journal of Structural Geology* 32, 1656-1667.
880

881 Henza, A.A., Withjack, M.O., Schlische, R.W., 2011. How do the properties of a pre-existing normal-fault
882 population influence fault development during a subsequent phase of extension? *Journal of Structural Geology*
883 33, 1312-1324.
884

885 Holgate, N.E., Jackson, C.A.-L., Hampson, G.J., Dreyer, T., 2013. Sedimentology and sequence stratigraphy of the
886 Middle-upper Jurassic Krossfjord and Fensfjord formations, troll Field, northern north Sea. *Petroleum Geoscience*
887 19, 237-258.
888

889 Hongxing, G., Anderson, J.K., *Fault Throw Profile and Kinematics of Normal Fault.-Conceptual Models and
890 Geologic Examples*. 2007. *Geological Journal of China Universities*. 13, 75-88.
891

892 Imber, J., Holdsworth, R., McCaffrey, K., Wilson, R., Jones, R., England, R., Gjeldvik, G., 2005. Early Tertiary sinistral
893 transpression and fault reactivation in the western Vøring Basin, Norwegian Sea: Implications for hydrocarbon
894 exploration and pre-breakup deformation in ocean margin basins. *AAPG bulletin* 89, 1043-1069.
895

896 Keep, M., McClay, K., 1997. Analogue modelling of multiphase rift systems. *Tectonophysics* 273, 239-270.
897

898 Knudsen, B.-E., Liljedahl, T., Midtbøe, P., Søderstrøm, B., 1997. Oblique rifting and sequential faulting in the Jurassic
899 development of the northern North Sea. *Journal of Structural Geology* 19, 1285-1302.
900

901 Kornsawan, A., Morley, C.K., 2002. The origin and evolution of complex transfer zones (graben shifts) in conjugate
902 fault systems around the Funan Field, Pattani Basin, Gulf of Thailand. *Journal of Structural Geology* 24, 435-449.
903

904 Krantz, R.W., 1989. Orthorhombic fault patterns: The odd axis model and slip vector orientations. *Tectonics* 8, 483-
905 495.
906

907 Kyrkjebø, R., Gabrielsen, R., Faleide, J., 2004. Unconformities related to the Jurassic–Cretaceous synrift–post-rift
908 transition of the northern North Sea. *Journal of the Geological Society* 161, 1-17.
909

910 Lepercq, J.-Y., Gaulier, J.-M., 1996. Two-stage rifting in the North Viking Graben area (North Sea): inferences from
911 a new three-dimensional subsidence analysis. *Marine and Petroleum Geology* 13, 129-148.
912

913 Lervik, K.-S., 2006. Triassic lithostratigraphy of the northern North Sea Basin. *Norsk Geologisk Tidsskrift* 86, 93-116.
914

915 Lezzar, K.E., Tiercelin, J.-J., Le Turdu, C., Cohen, A.S., Reynolds, D.J., Le Gall, B., Scholz, C.A., 2002. Control of normal
916 fault interaction on the distribution of major Neogene sedimentary depocenters, Lake Tanganyika, East African
917 rift. *AAPG Bulletin* 86, 1027-1060.
918

919 Long, J., Imber, J., 2010. Geometrically coherent continuous deformation in the volume surrounding a seismically
920 imaged normal fault-array. *Journal of Structural Geology* 32, 222-234.
921

922 Maerten, L., Gillespie, P., Pollard, D.D., 2002. Effects of local stress perturbation on secondary fault development.
923 *Journal of Structural Geology* 24, 145-153.
924

925 Maerten, L., Willemsse, E.J., Pollard, D.D., Rawnsley, K., 1999. Slip distributions on intersecting normal faults. *Journal*
926 *of Structural Geology* 21, 259-272.
927

928 Manighetti, I., King, G., Gaudemer, Y., 2001. Slip accumulation and lateral propagation of active. *Journal of*
929 *Geophysical Research* 106, 13,667-13,696.
930

931 Mansfield, C.S., Cartwright, J.A., 1996. High resolution fault displacement mapping from three-dimensional seismic
932 data: evidence for dip linkage during fault growth. *Journal of Structural Geology* 18, 249-263.
933

934 McClay, K.R., White, M.J., 1995. Analogue modelling of orthogonal and oblique rifting. *Marine and Petroleum*
935 *Geology* 12, 137-151.
936

937 McLeod, A.E., Underhill, J.R., Davies, S.J., Dawers, N.H., 2002. The influence of fault array evolution on synrift
938 sedimentation patterns: Controls on deposition in the Strathspey-Brent-Statfjord half graben, northern North Sea:
939 *AAPG Bulletin* 86, 1061-1094.
940

941 Meyer, V., Nicol, A., Childs, C., Walsh, J., Watterson, J., 2002. Progressive localisation of strain during the evolution
942 of a normal fault population. *Journal of Structural Geology* 24, 1215-1231.
943

944 Morley, C., 2007. Variations in late Cenozoic–Recent strike-slip and oblique-extensional geometries, within
945 Indochina: The influence of pre-existing fabrics. *Journal of Structural Geology* 29, 36-58.
946

947 Morley, C., Haranya, C., Phoosongsee, W., Pongwapee, S., Kornsawan, A., Wonganan, N., 2004. Activation of rift
948 oblique and rift parallel pre-existing fabrics during extension and their effect on deformation style: examples from
949 the rifts of Thailand. *Journal of Structural Geology* 26, 1803-1829.
950

951 Muraoka, H., Kamata, H., 1983. Displacement distribution along minor fault traces. *Journal of Structural Geology* 5,
952 483-495.
953

954 Needham, D., Yielding, G., Freeman, B., 1996. Analysis of fault geometry and displacement patterns. *Geological*
955 *Society, London, Special Publications* 99, 189-199.

956
957 Nicol, A., Watterson, J., Walsh, J.J., Childs, C., 1996. The shapes, major axis orientations and displacement patterns
958 of fault surfaces. *Journal of Structural Geology* 18, 235-248.
959
960 Nelson, M. 2006. 3D Geometry and Kinematics of Non-Colinear Fault Intersections. Unpublished PhD Thesis.
961 Cardiff University
962
963 Nixon, C.W., Sanderson, D.J., Dee, S.J., Bull, J.M., Humphreys, R.J., Swanson, M.H., 2014. Fault interactions and
964 reactivation within a normal fault network at Milne Point, Alaska. *AAPG Bulletin*. 98, 2081-2107.
965
966 Odinsen, T., Reemst, P., Van Der Beek, P., Faleide, J.I., Gabrielsen, R.H., 2000. Permo-Triassic and Jurassic extension
967 in the northern North Sea: results from tectonostratigraphic forward modelling. *Geological Society, London,*
968 *Special Publications* 167, 83-103.
969
970 Peacock, D.C.P., Sanderson, D.J., 1991. Displacements, segment linkage and relay ramps in normal fault zones.
971 *Journal of Structural Geology* 13, 721-733.
972
973 Pochat, S., Castelltort, S., Choblet, G., Van Den Driessche, J., 2009. High-resolution record of tectonic and
974 sedimentary processes in growth strata. *Marine and Petroleum Geology* 26, 1350-1364.
975
976 Rattey, R., Hayward, A., 1993. Sequence stratigraphy of a failed rift system: the Middle Jurassic to Early Cretaceous
977 basin evolution of the Central and Northern North Sea, *Geological Society, London, Petroleum Geology*
978 *Conference series. Geological Society of London*, pp. 215-249.
979
980 Reches, Z.e., 1987. Determination of the tectonic stress tensor from slip along faults that obey the Coulomb yield
981 condition. *Tectonics* 6, 849-861.
982
983 Reeve, M.T., Bell, R.E., Duffy, O.B., Jackson, C.A-L., Sansom, E., 2015. The Growth of Non-Colinear Fault Systems;
984 What Can We Learn From 3D Seismic Reflection Data? *Journal of Structural Geology*. 70, 141-155.

985 Roberts, A., Yielding, G., Kusznir, N., Walker, I., Dorn-Lopez, D., 1993. Mesozoic extension in the North Sea:
986 constraints from flexural backstripping, forward modelling and fault populations, *Geological Society, London,*
987 *Petroleum Geology Conference series. Geological Society of London*, 1123-1136.
988
989 Roberts, A., Yielding, G., Kusznir, N., Walker, I., Dorn-Lopez, D., 1995. Quantitative analysis of Triassic extension in
990 the northern Viking Graben. *Journal of the Geological Society* 152, 15-26.
991
992 Sinclair, I., Withjack, M., 2008. Mid to Late Cretaceous structural and sedimentary architecture at the Terra Nova
993 Oilfield, offshore Newfoundland—implications for the tectonic history of the North Atlantic. *Central Atlantic*
994 *Conjugate Margins*, 125-141.
995
996 Smethurst, M., 2000. Land-offshore tectonic links in western Norway and the northern North Sea. *Journal of the*
997 *Geological Society* 157, 769-781.
998
999 Stewart, I.J., Rattey, R.P. & Vann, I.R. (1992) Structural style and the habit of hydrocarbons in the North Sea. In:
1000 *Structural and Tectonic Modelling and its Application to Petroleum Geology* (Ed. by R.M. Larsen, H. Brekke, B.T.
1001 *Larsen & E. Talleraas*) NPF Spec. Publ.,1, 197-220
1002
1003 Stewart, S.A., 2001. Displacement distributions on extensional faults: Implications for fault stretch, linkage, and
1004 seal. *AAPG Bulletin* 85, 587-599.
1005
1006 Stewart, S.A., Clark, J.A., 1999. Impact of salt on the structure of the Central North Sea hydrocarbon fairways.
1007 *Petroleum Geology Conference Series, Geological Society, London*. 5, 179-200.
1008
1009 Ter Voorde, M., Faerseth, R., Gabrielsen, R., Cloetingh, S., 2000. Repeated lithosphere extension in the northern
1010 Viking Graben: a coupled or decoupled rheology? *Special Publication-Geological Society of London* 167, 59-82.
1011

1012 Trudgill, B.D., 2002. Structural controls on drainage development in the Canyonlands grabens of southeast Utah.
1013 AAPG Bulletin 86, 1095-1112.
1014
1015 Underhill, J.R., Partington, M.A., 1993. Jurassic thermal doming and deflation in the North Sea: implications of the
1016 sequence stratigraphic evidence. Geological Society of London. 4, 337-345.
1017
1018 Vetti, V.V., Fossen, H., 2012. Origin of contrasting Devonian supradetachment basin types in the Scandinavian
1019 Caledonides. Geology 40, 571-574.
1020
1021 Walsh, J., Nicol, A., Childs, C., 2002. An alternative model for the growth of faults. Journal of Structural Geology 24,
1022 1669-1675.
1023
1024 Walsh, J.J., Watterson, J., 1989. Displacement gradients on fault surfaces. Journal of Structural Geology 11, 307-
1025 316.
1026
1027 Walsh, J.J., Watterson, J., 1991. Geometric and kinematic coherence and scale effects in normal fault systems.
1028 Geological Society, London, Special Publications 56, 193-203.
1029
1030 Watterson, J., 1986. Fault dimensions, displacements and growth. Pure and Applied Geophysics 124, 365-373.
1031
1032 Whipp, P., Jackson, C.L., Gawthorpe, R., Dreyer, T., Quinn, D., 2014. Fault array evolution above a reactivated rift
1033 fabric; a subsurface example from the northern Horda Platform fault array, Norwegian North Sea. Basin Research.
1034 26, 523-549.
1035
1036 Wilson, P., Elliott, G.M., Gawthorpe, R.L., Jackson, C.A.-L., Michelsen, L., Sharp, I.R., 2013. Geometry and
1037 segmentation of an evaporite-detached normal fault array: 3D seismic analysis of the southern Bremstein Fault
1038 Complex, offshore mid-Norway. Journal of Structural Geology. 51, 74-91.
1039
1040 Young, M.J., Gawthorpe, R.L., Hardy, S., 2001. Growth and linkage of a segmented normal fault zone; the Late
1041 Jurassic Murchison-Statfjord North Fault, northern North Sea. Journal of Structural Geology 23, 1933-1952.
1042
1043 Ziegler, P.A., 1975. Geologic evolution of North Sea and its tectonic framework. AAPG Bull 59, 1073-1097.
1044
1045 Ziegler, P.A., 1982. Triassic rifts and facies patterns in Western and Central Europe. International Journal of Earth
1046 Sciences 71, 747-772.
1047
1048 Ziegler, P.A., 1990. Tectonic and palaeogeographic development of the North Sea rift system. Tectonic Evolution
1049 of the North Sea Rifts. Clarendon Press, Oxford, 1-36.
1050
1051 Ziegler, P., 1992. North Sea rift system. Tectonophysics 208, 55-75.
1052

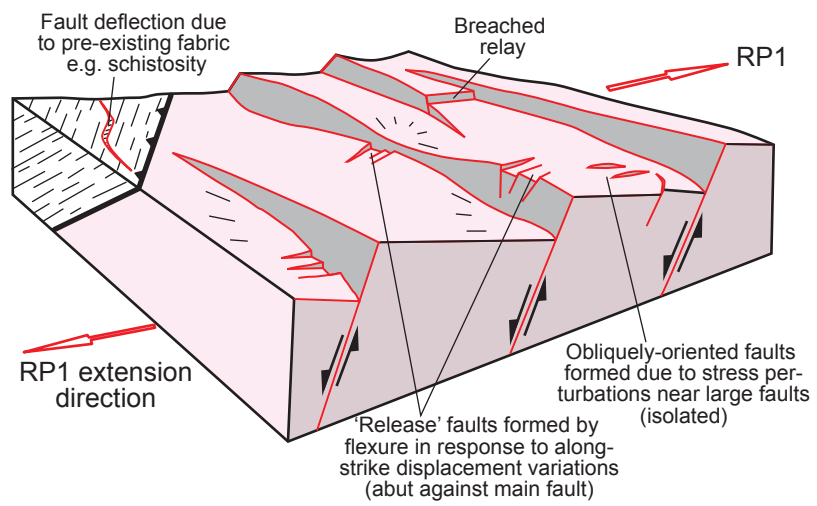


Figure 1

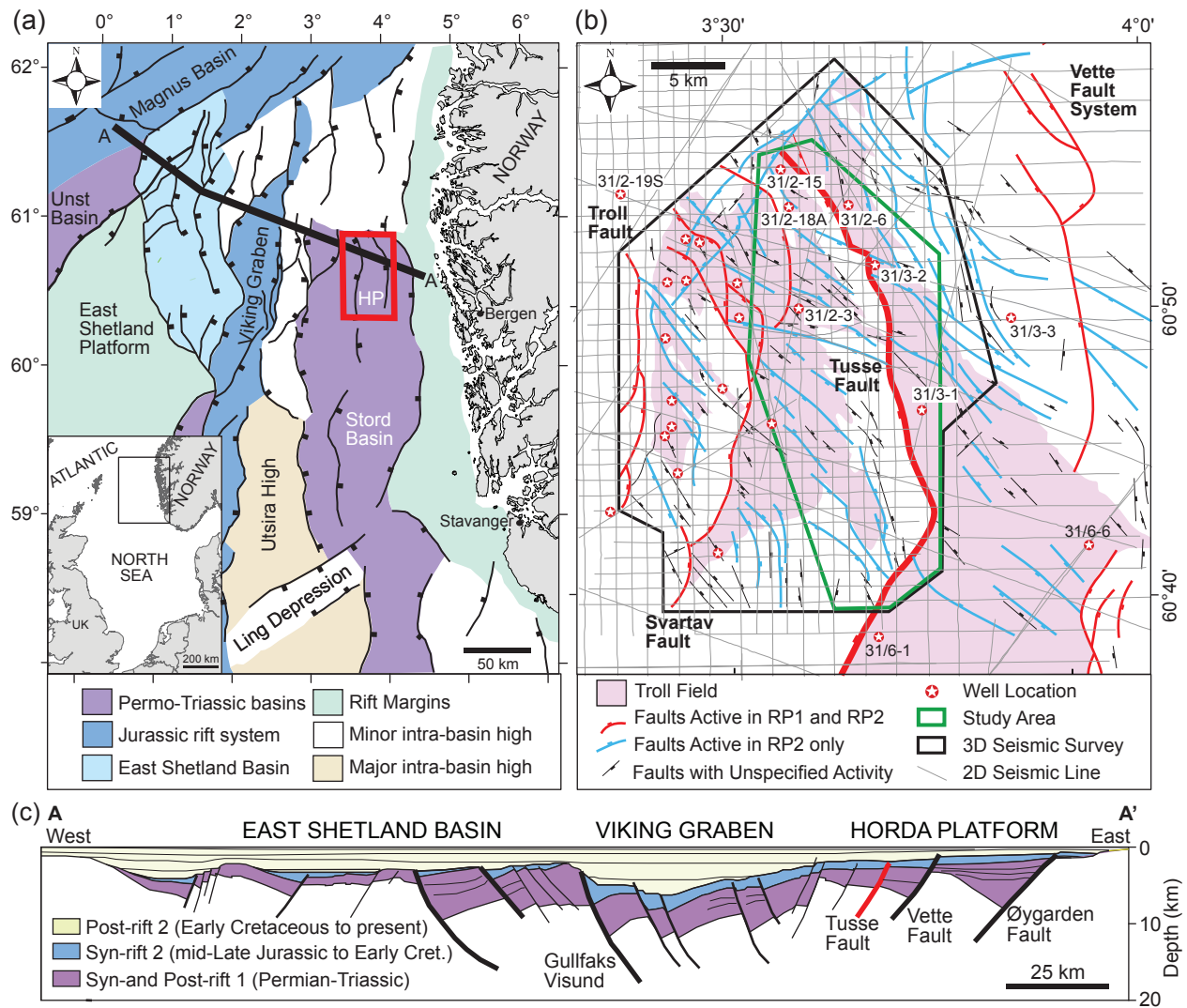


Figure 2

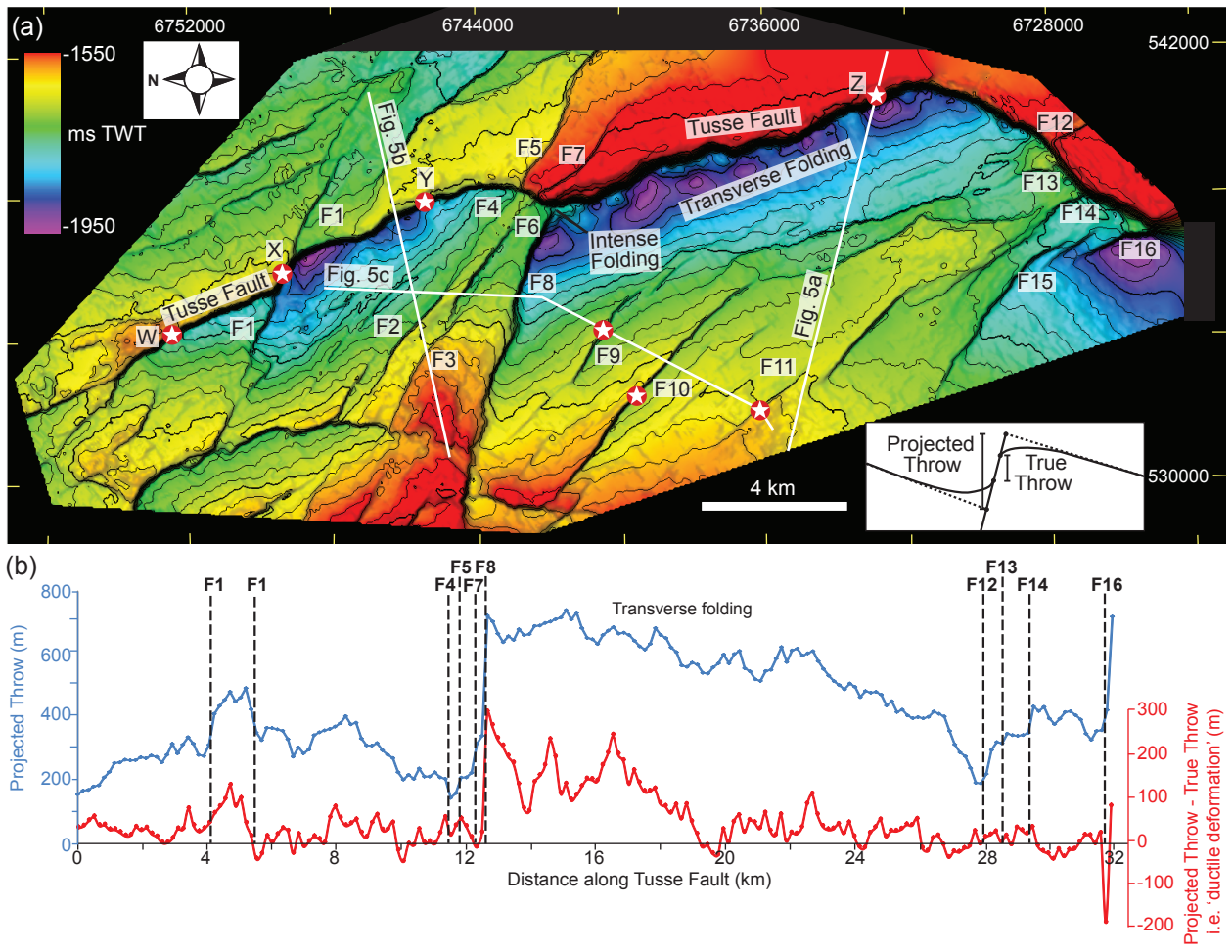


Figure 4

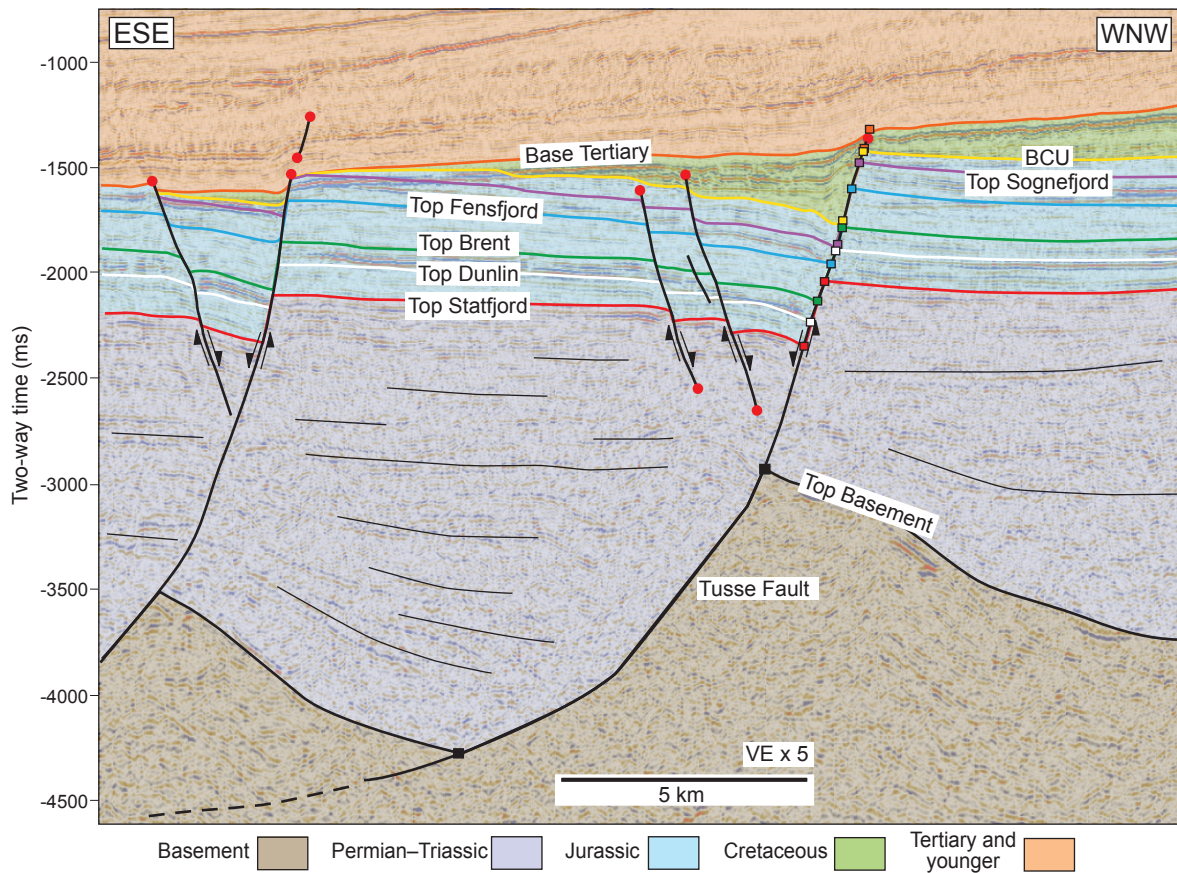
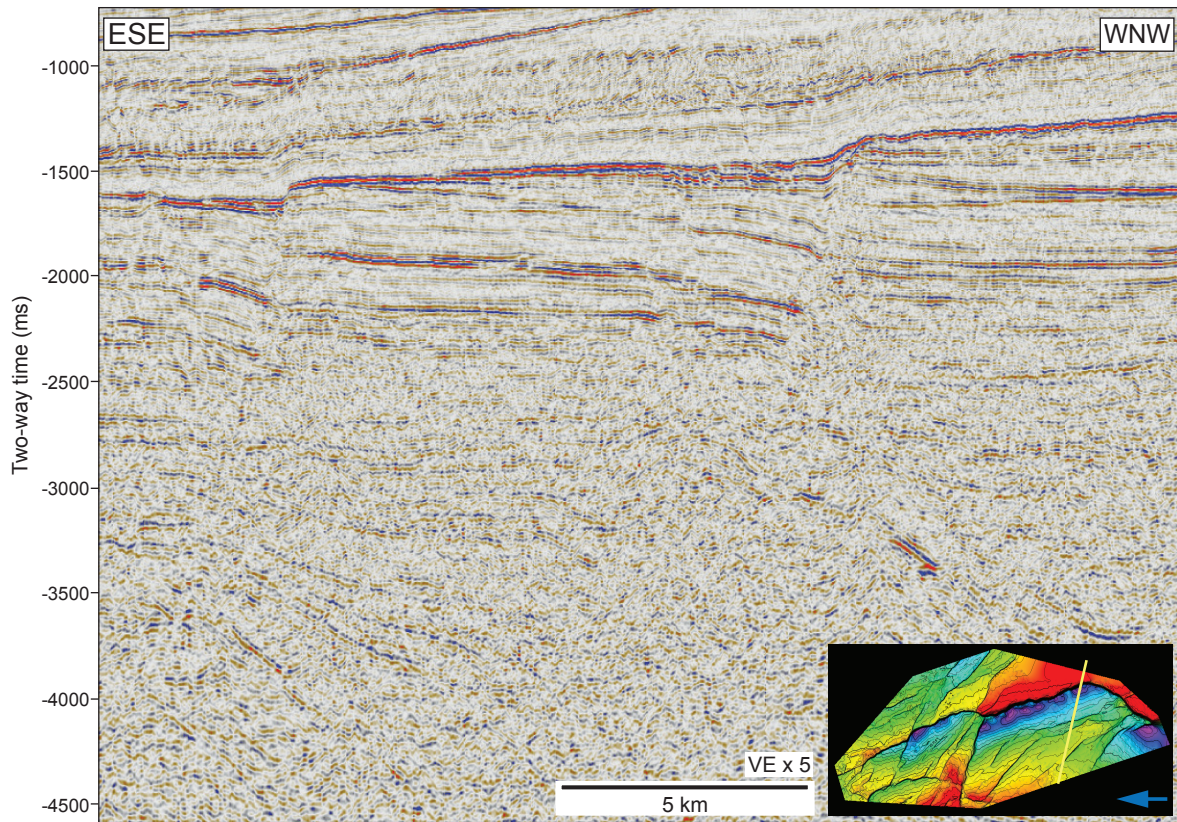


Figure 5a

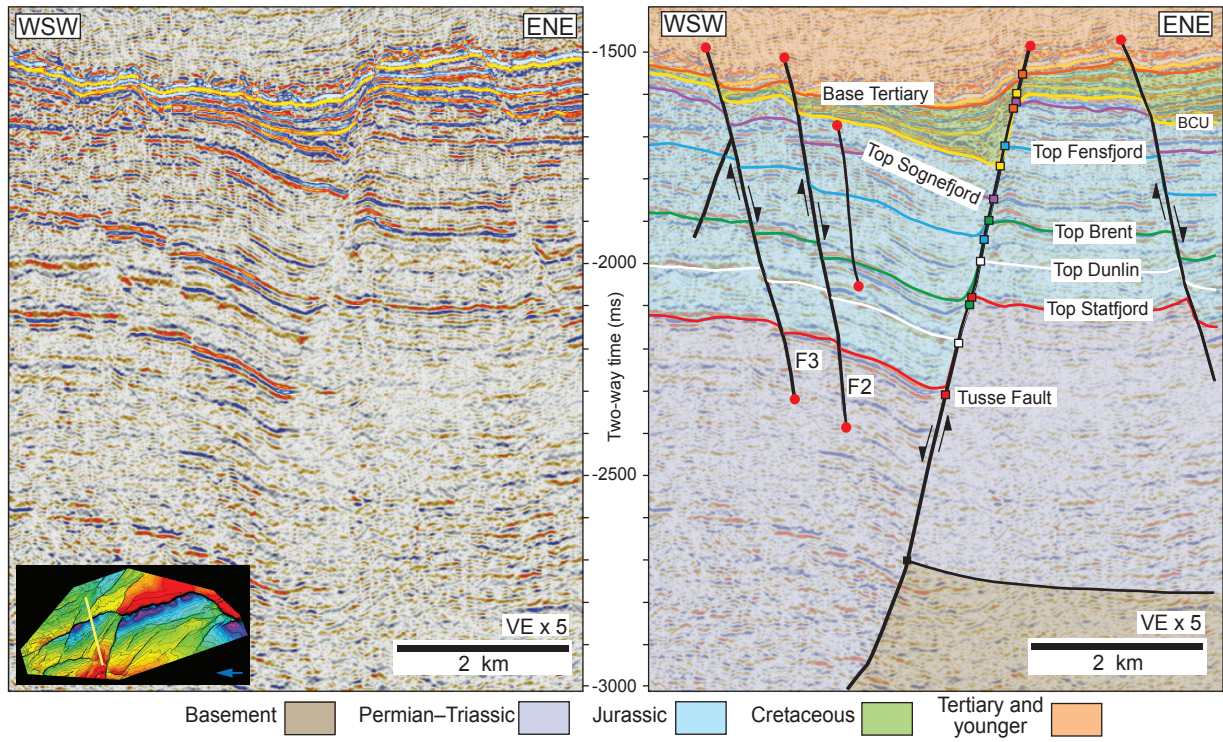


Figure 5b

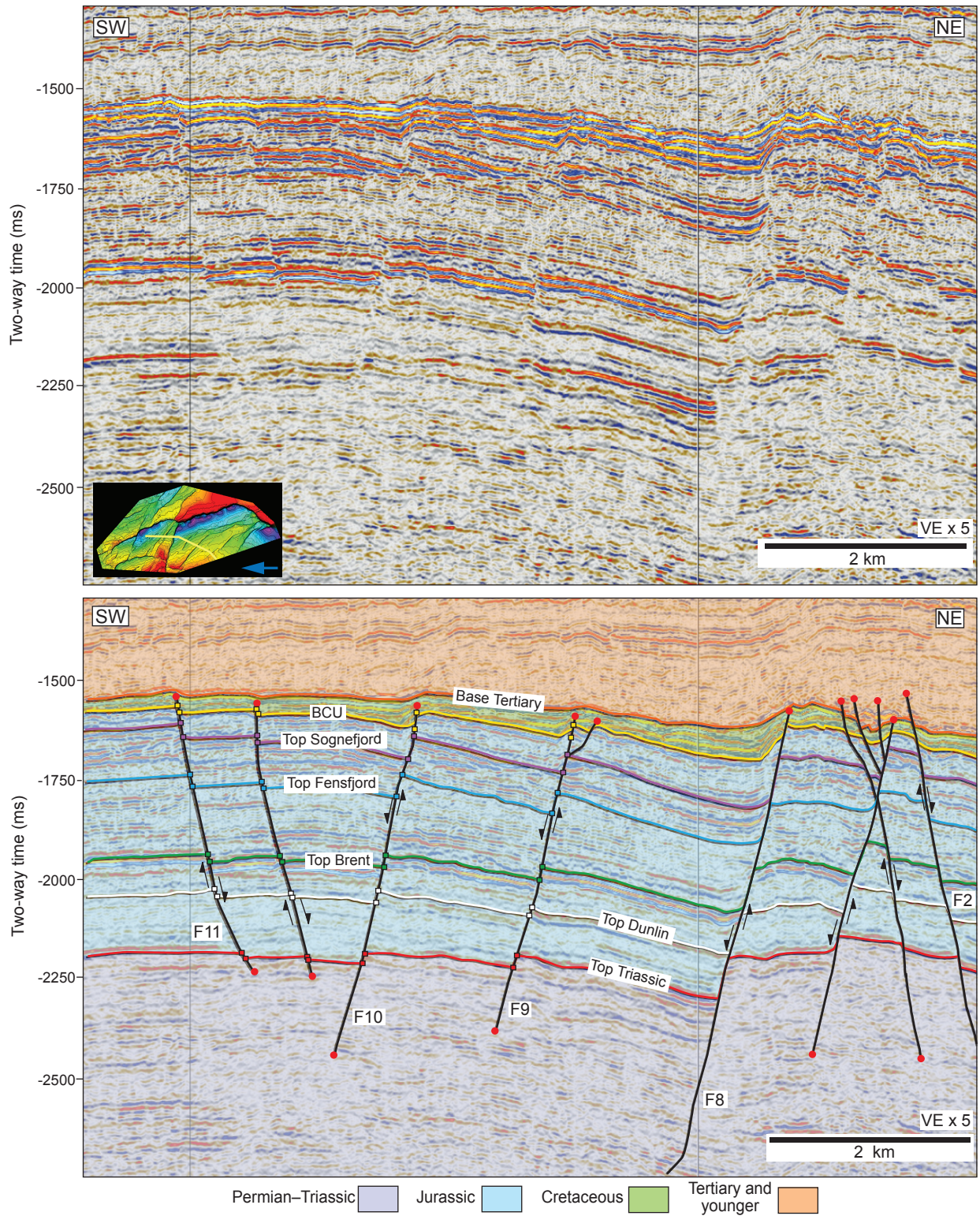


Figure 5c

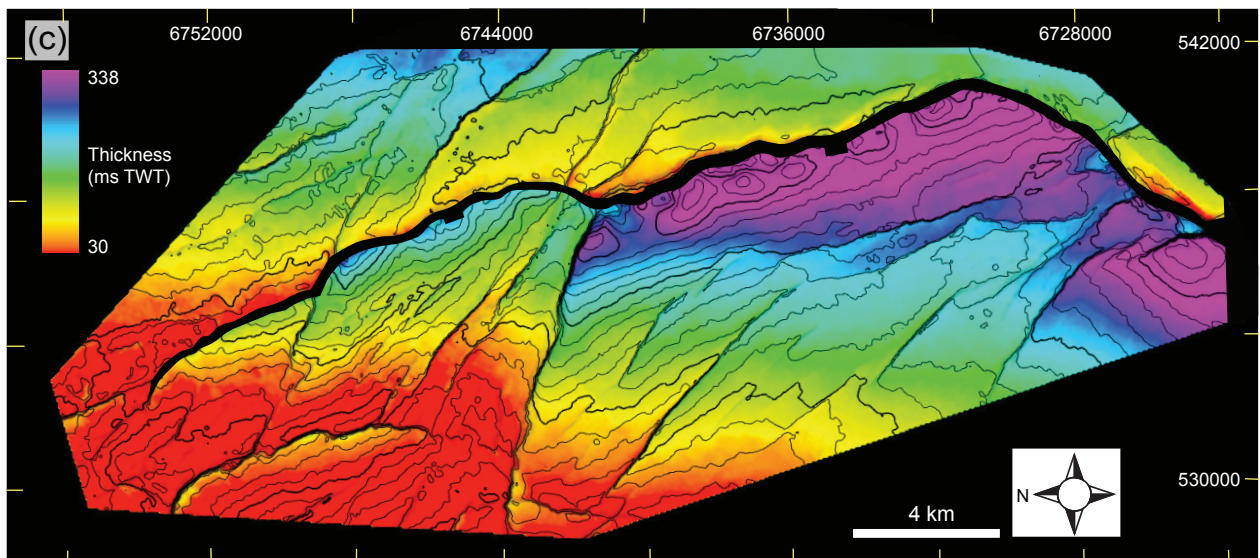
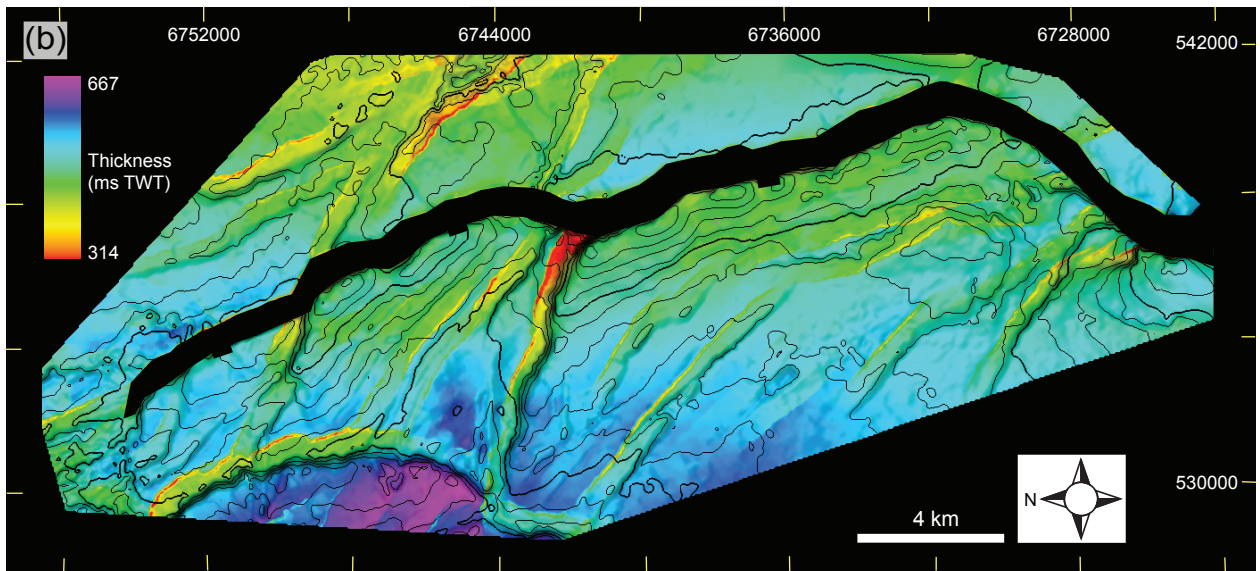
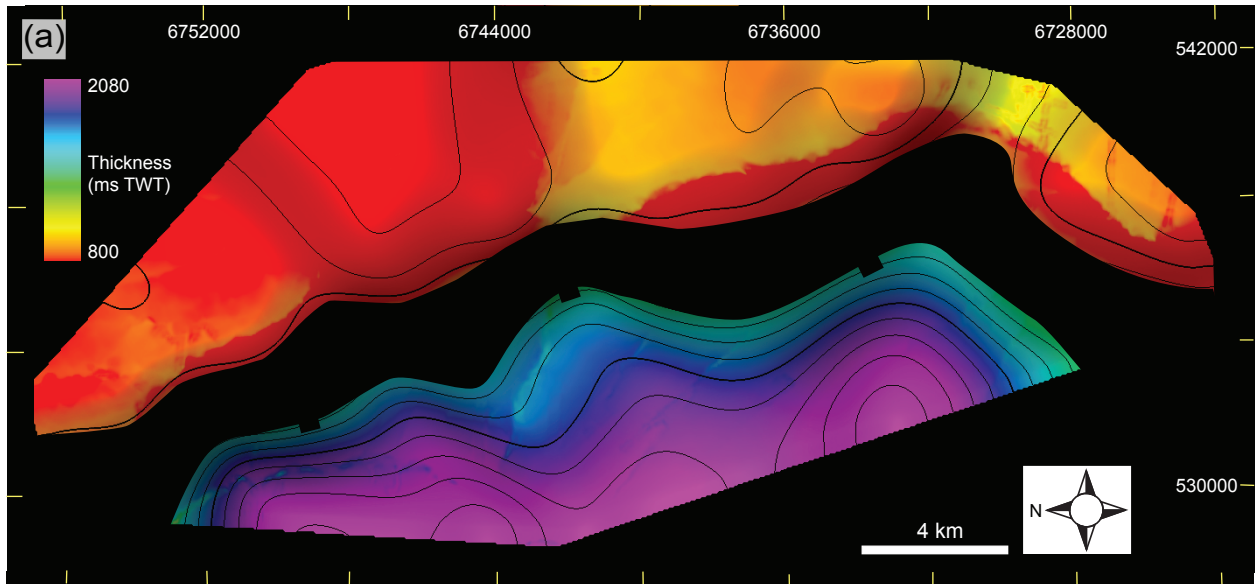


Figure 6

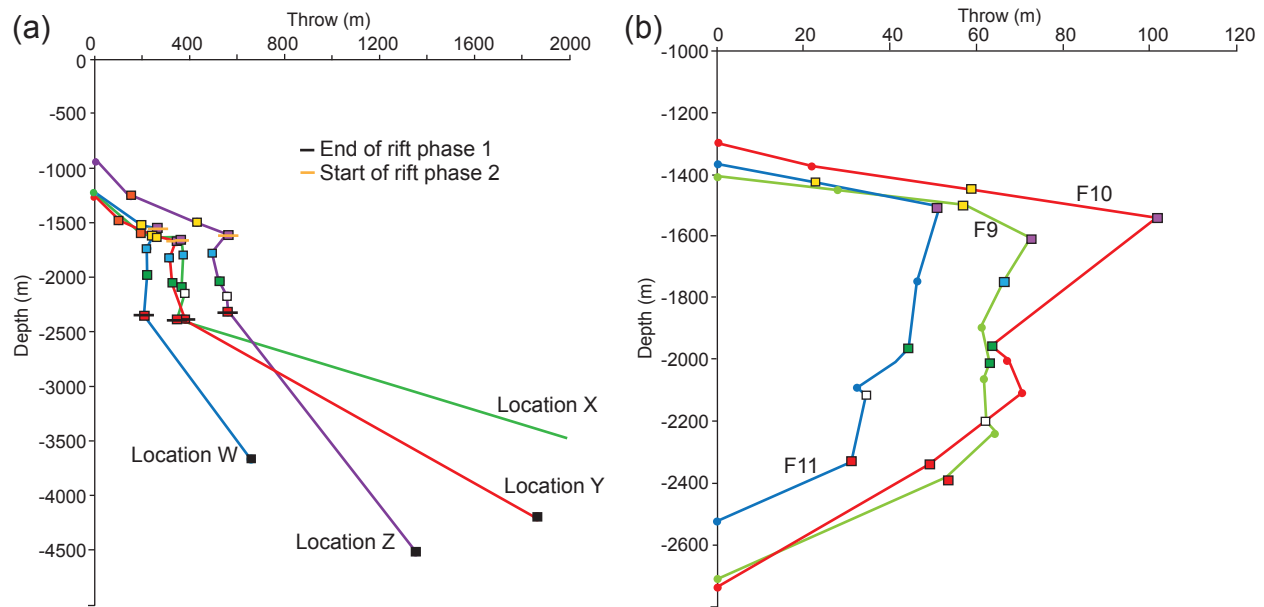


Figure 7

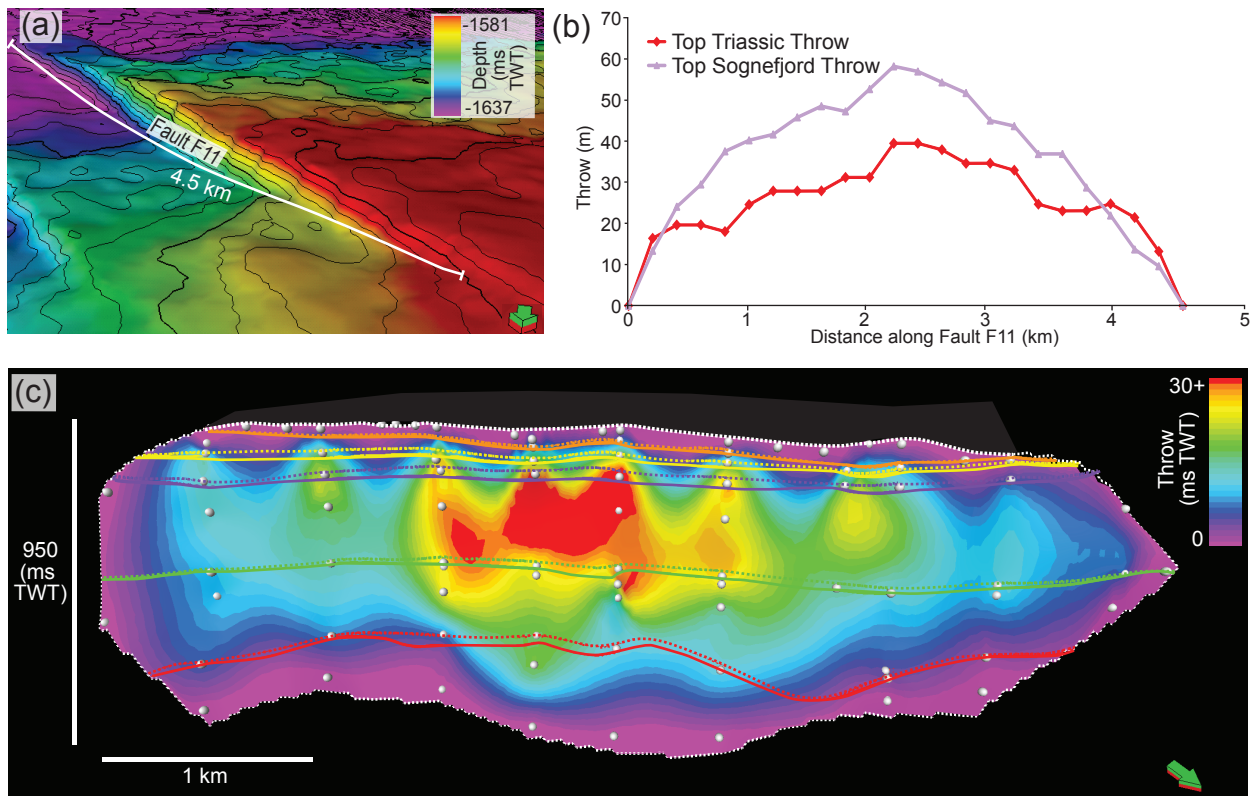


Figure 8

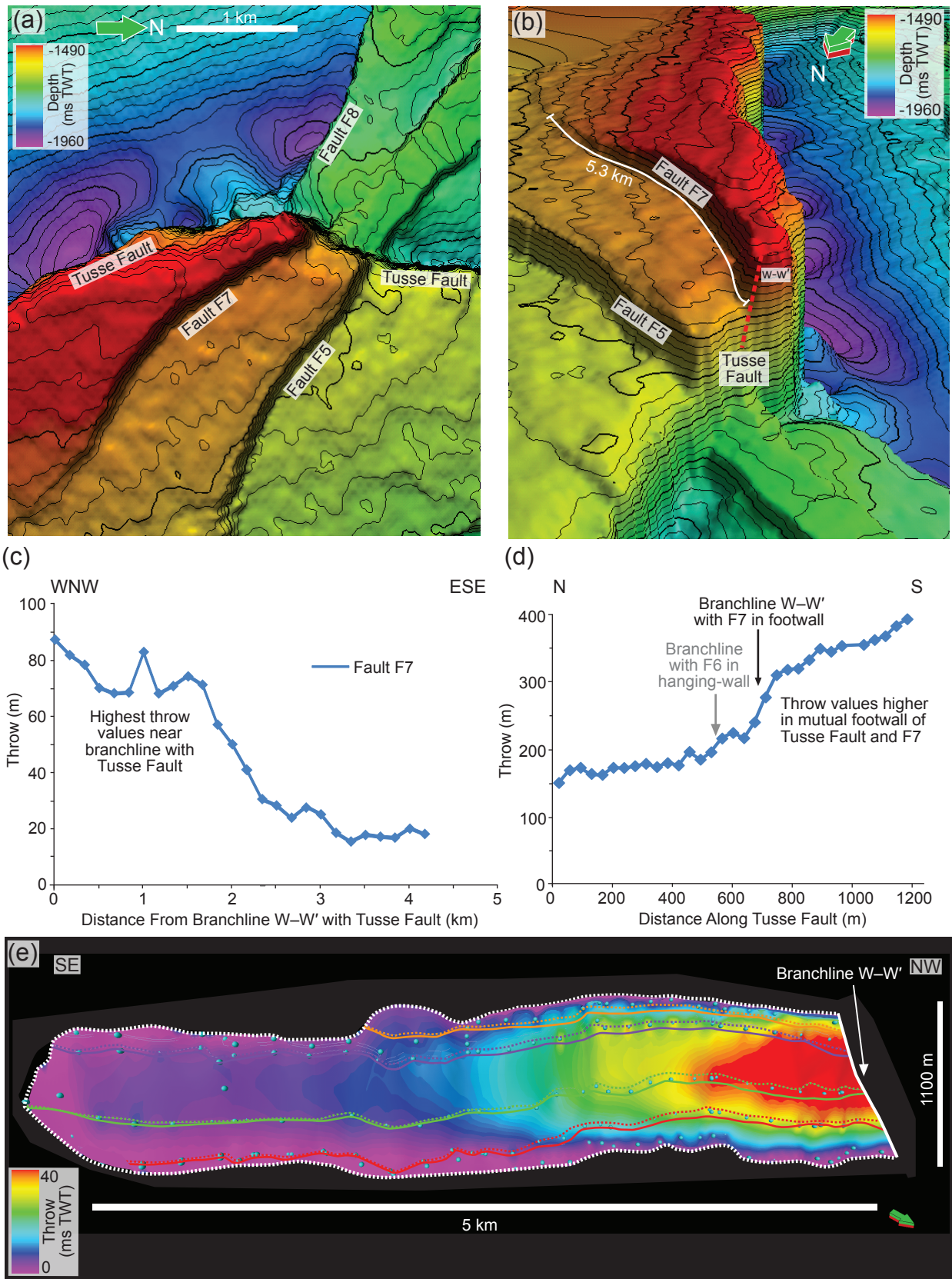


Figure 9

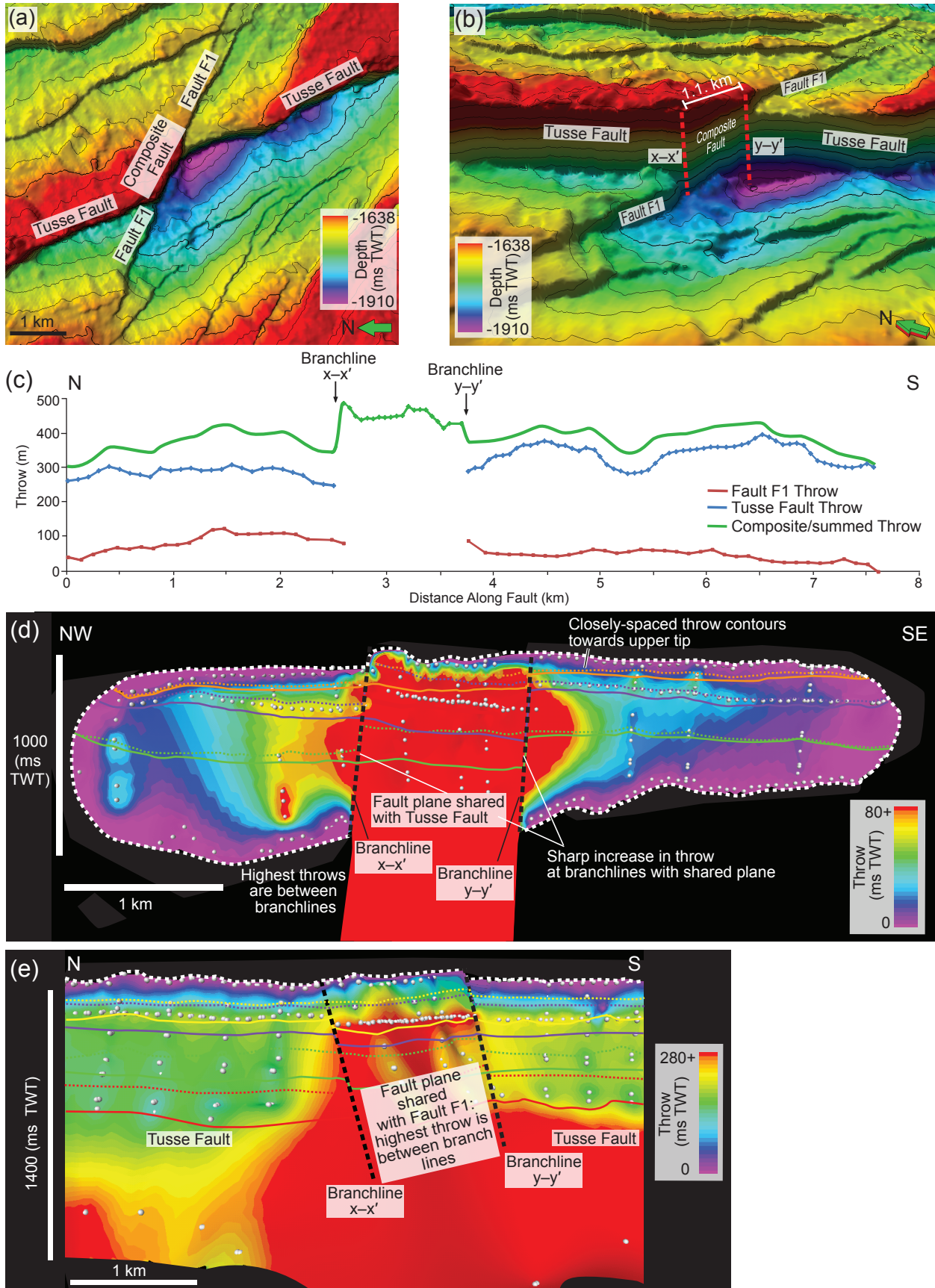


Figure 10

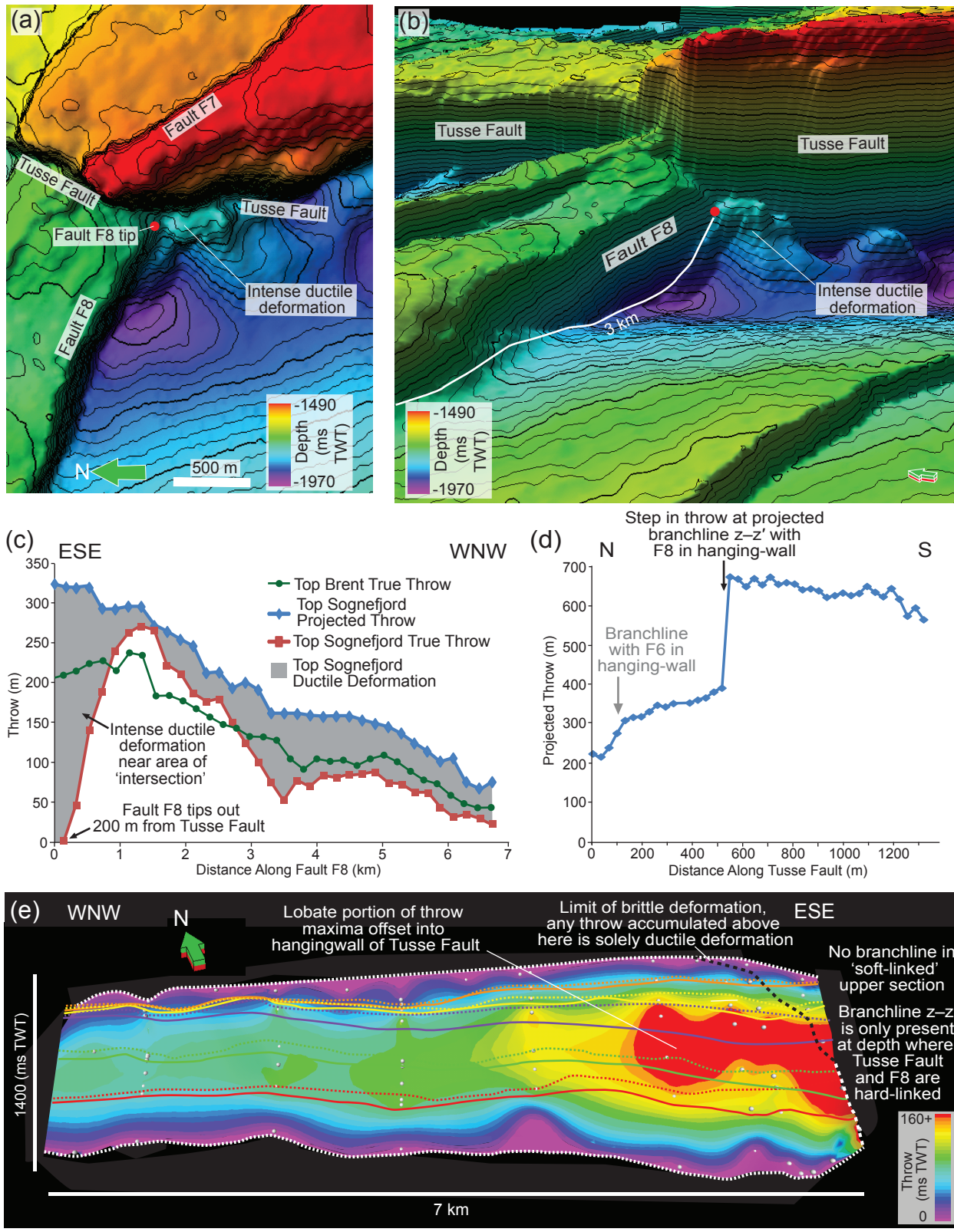


Figure 11

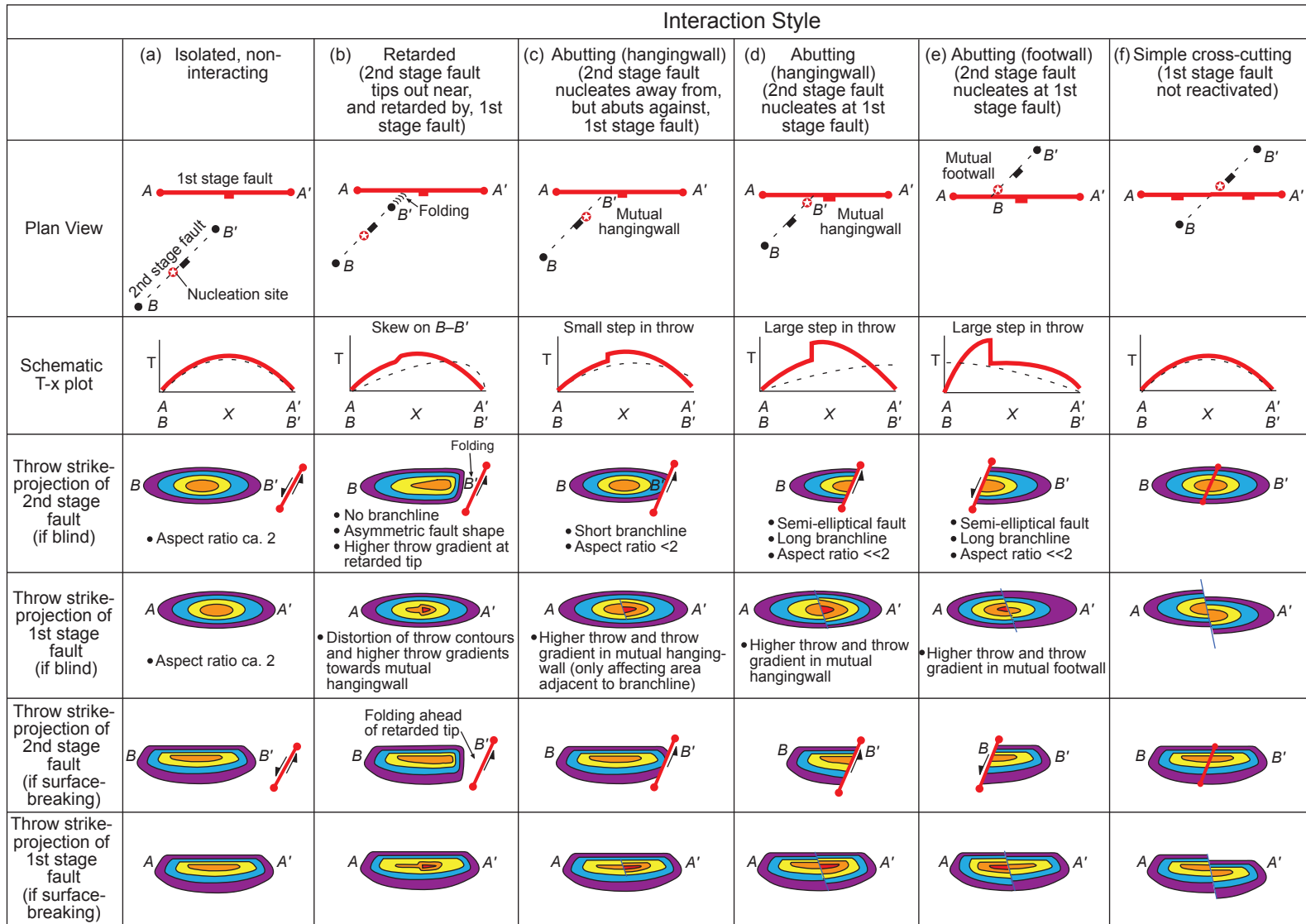


Figure 12

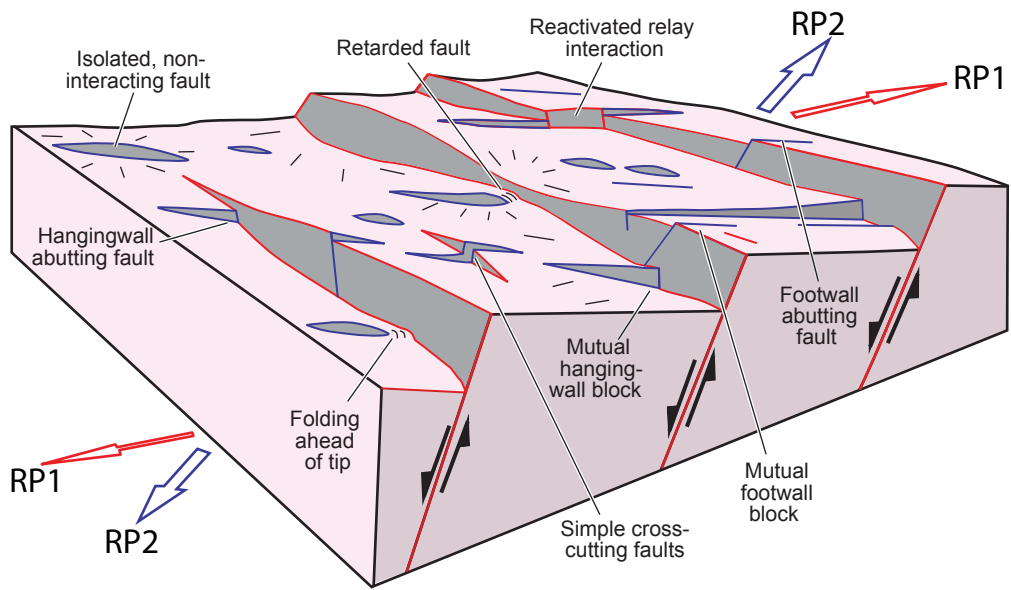


Figure 13